⏾The Influence of Atmospheric Convection on the Interaction between the Indian Ocean and ENSO

Claudia E. Wieners, Henk A. Dijkstra, and Will P. M. de Ruijter

Institute for Marine and Atmospheric Research Utrecht, Department of Physics and Astronomy,
Utrecht University, Utrecht, Netherlands

ABSTRACT

In recent years it has been proposed that a negative (positive) Indian Ocean dipole (IOD) in boreal autumn favors an El Niño (La Niña) at a lead time of 15 months. Observational analysis suggests that a negative IOD might be accompanied by easterly anomalies over the western Pacific. Such easterlies can enhance the western Pacific warm water volume, thus favoring El Niño development from the following boreal spring onward. However, a Gill-model response to a negative IOD forcing would lead to nearly zero winds over the western Pacific. The authors hypothesize that a negative IOD—or even a cool western Indian Ocean alone—leads to low-level air convergence and hence enhanced convectional heating over the Maritime Continent, which in turn amplifies the wind convergence so as to cause easterly winds over the western Pacific. This hypothesis is tested by coupling an idealized Indian Ocean model and a convective feedback model over the Maritime Continent to the Zebiak–Cane model. It is found that, for a sufficiently strong convection feedback, a negative (positive) IOD indeed forces easterlies (westerlies) over the western Pacific. The contribution from the eastern IOD pole dominates. IOD variability is found to destabilize the El Niño–Southern Oscillation (ENSO) mode, whereas Indian Ocean basinwide warming (IOB) variability dampens ENSO, even in the presence of convection. The influence of the Indian Ocean on the spectral properties of ENSO is dominated by the IOB, while the IOD is a better predictor for individual ENSO events.

1. Introduction

Skillful predictions of the different phases of El Niño–Southern Oscillation (ENSO) are still a challenge for the climate research community. While the basic processes in the equatorial Pacific Ocean are reasonably well understood (see, e.g., Philander 1990; Neelin et al. 1998; Zebiak and Cane 1987), the degree to which the extratropical Pacific, the Atlantic Ocean, and the Indian Ocean (IO) affect ENSO is still an active field of research. In this study we will focus on the influence of the Indian Ocean transmitted via the atmosphere (the "atmospheric bridge").

In the Indian Ocean, two modes of variability have been identified: the Indian Ocean basinwide warming (IOB; Klein et al. 1999) and the Indian Ocean dipole (IOD) (Webster et al. 1999; Saji et al. 1999). Both IOB and IOD may be influenced by and in turn have influence on ENSO. The IOB is the dominant Indian Ocean response to ENSO, with Indian Ocean SST peaking in boreal spring following El Niño (Klein et al. 1999). The IOB in turn is thought to dampen ENSO and increase its frequency, as a warming Indian Ocean causes easterlies over the western Pacific (Gill 1980), which counteract the westerlies associated with the ongoing El Niño and initiate a switch to La Niña (see, e.g., Kug and Kang 2006; Kug et al. 2006; Santoso et al. 2012; Kajtar et al. 2017). While these studies relied on GCMs and observations, Wieners et al. (2017) confirmed their results with an intermediate-complexity model. The IOB does not offer much additional predictive skill, possibly because the IOB depends so strongly on ENSO that it can be regarded as part of the ENSO cycle (Xie et al. 2009; Izumo et al. 2014).

The relation between the IOD and ENSO is less clear. Throughout this study we define as year 1 the year wherein El Niño develops (peaking in the boreal winter of year 1/2). A positive IOD [i.e., a warm western Indian

---

Corresponding author: Claudia E. Wieners, c.e.wieners@uu.nl

Ocean (WIO) and cool eastern Indian Ocean (EIO)],[1] often occurs in the boreal autumn of year 1 but can also occur independently of ENSO (Schott et al. 2009, section 4.2; Webster et al. 1999). It has been argued that the Gill response of the two poles of the IOD over the Pacific nearly cancels, due to their close proximity, but that an IOD co-occurring with El Niño (i.e., in autumn/winter of year 1) can indirectly strengthen it by reducing the damping effect of the IOB (Annamalai et al. 2005; Santoso et al. 2012). Izumo et al. (2015) proposed a mechanism by which the IOD in autumn(year 0) can impact ENSO in winter(1/2): in autumn(0), the wind effects of the cool western and warm eastern Indian Ocean over the western Pacific cancel, but in the spring(1), when the eastern pole also cools (so as to yield a pure IOB pattern), the resulting westerlies cause a downwelling Kelvin wave that might initiate El Niño, without being partially compensated by the delayed negative feedback that would arise if the IOB-induced westerlies had already been present in autumn. However, Izumo et al. (2010, 2014) suggest that a negative IOD is associated with easterlies over the western Pacific. Wieners et al. (2016) found in observational data that a cool western Indian Ocean in autumn(0) is accompanied by easterlies over the western Pacific. These are significant (but only at 80% confidence) even if the effect of a decaying La Niña (winter −1/0) is regressed out. Such easterlies lead to a significant increase in warm water volume (WWV); the correlation between autumn western Indian Ocean SST and WWV a few months later is significant (Wieners et al. 2016). A high WWV in turn is a prerequisite to El Niño (Wyrtki 1975; Jin 1997; Meinen and McPhaden 2000). Note that although we use a negative IOD as example, a positive IOD might likewise induce La Niña.

But how does the negative IOD or cool western Indian Ocean cause easterlies over the western Pacific, while based on the Gill response one would expect very little response in case of a negative IOD or westerlies in case of a cool western Indian Ocean (Fig. 1a)? In case of the IOD, Izumo et al. (2010, 2014) suggest that SST anomalies in the eastern pole have a stronger effect on the atmosphere because the eastern pole lies under a region of high humidity, where convective precipitation is most sensitive to SST anomalies.

However, Wieners et al. (2016) found that the western Indian Ocean in autumn(0) contains more information on ENSO in winter(1/2) than the eastern Indian Ocean. They conjectured that the weak upward motion above the east Indian Ocean and the Maritime Continent (MC) that is part of the Gill response to western Indian Ocean cooling can also be amplified by a positive convective feedback in the warm and moist air over the Indonesian warm pool (Fig. 1b). If the convection effect becomes strong enough, wind convergence near the ground arises, which leads to easterlies over the western Pacific. This hypothesis is in line with Watanabe and Jin (2002, 2003), who suggest that Indian Ocean warming during El Niño helps to suppress convection above the eastern Maritime Continent (although this convection anomaly may not overcome the Gill response due to local SST forcing). Also, Annamalai et al. (2010) suggest that SST and precipitation anomalies over the Maritime Continent influence ENSO. Note that if the SST anomaly is close to or even within the region with a warm, moist background state, the Gill response and nonlinear convection effect coact, as illustrated in Fig. 1c.

The aim of this study is to test whether nonlinear convection can indeed lead to easterly winds as a response to a negative IOD or even a cool western Indian Ocean. Next, we compare the effect of the IOD and IOB and assess the relative importance of the IOD poles to obtain a comprehensive overview of the impact of various Indian Ocean modes on ENSO. We use again the intermediate-complexity Zebiak–Cane model as in Wieners et al. (2017), to which we add a convective feedback representation over the warm pool. Similar idealized models have been used to investigate the effect of convection on the Indo-Pacific climatology and its stability (Anderson and McCreary 1985; Watanabe 2008), but we focus on the effect of Indian Ocean interannual variability on ENSO.

The model is described in section 2. In section 3 we investigate whether a simple convection feedback can lead to an easterly wind response over the western Pacific to western Indian Ocean cooling. We also consider the effects of other Indian Ocean modes of variability, mainly the IOB and IOD, on this wind response. A summary, discussion, and conclusions are provided in section 4.

2. Methods

The model used in this study is a two-basin extension of the Zebiak–Cane (ZC) model (Zebiak and Cane 1987). The basins are meridionally unbounded, and the Maritime Continent is modeled as a meridionally

---

[1] Note that throughout this paper by positive IOD we mean a warm western and cool eastern Indian Ocean, as obtained when regressing autumn Indian Ocean SST only onto the IOD index (Saji et al. 1999) and not mainly a cool eastern pole, as Izumo et al. (2015) and Shinoda et al. (2004) obtain by partial regression of SST onto IOD and IOB.
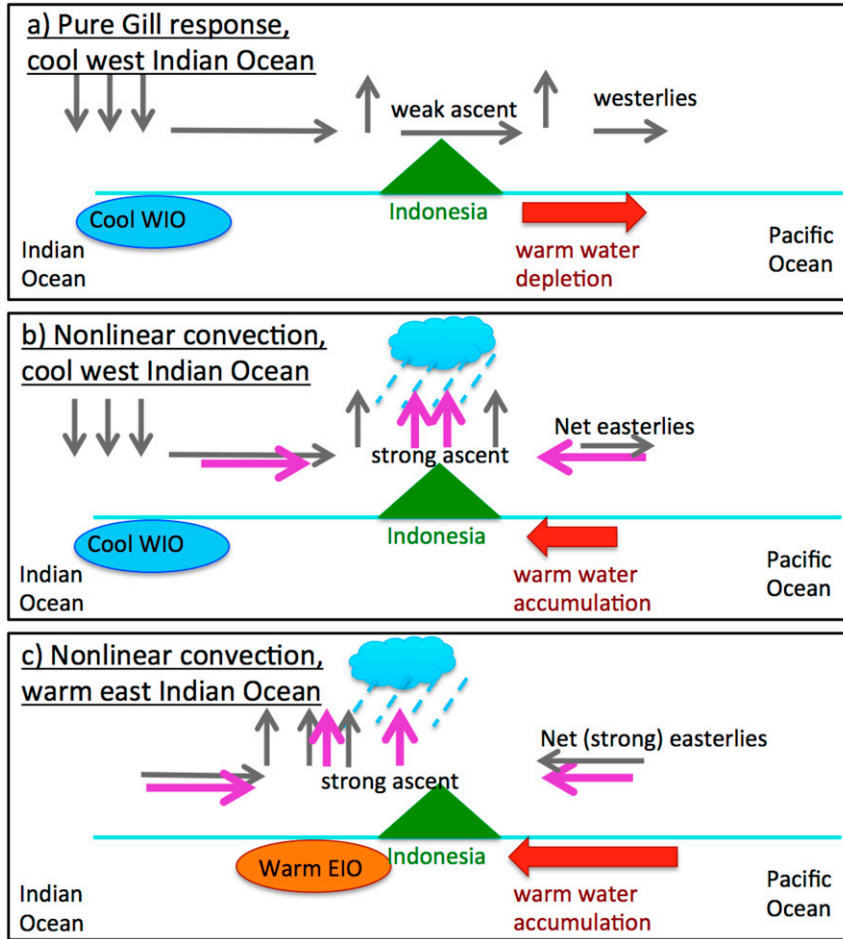
FIG. 1. Diagram of the mechanisms to be investigated. (a) Gill response to WIO cooling. The low SST leads to cooling, subsidence, and surface divergence of the air over the WIO; hence, to the east of the WIO, westerly anomalies and upward motion prevail. The westerlies may cause a depletion of the western Pacific WWV. (b) If the upward motion induced by the Gill response (gray arrows) is amplified by convective heating over the warm and moist Maritime Continent, surface convergence is induced there (purple arrows). If this effect is strong enough, it might overcome the Gill-induced westerlies and lead to net easterly anomalies over the western Pacific, which in turn may build up the WWV. (c) If the SST anomaly is in the EIO, such that it is close to or even overlaps with the region with a warm and moist background state, Gill response (gray) and convection-induced upward motion (purple) coact; hence, a warm eastern Indian Ocean is also expected to yield easterlies over the western Pacific.

unbounded block with meridional coasts and width $L_{MC} = L_I/2 = L_P/4$, where L_I and L_P are the widths of the Indian and Pacific Oceans, respectively (see Fig. 2 and Table 1). Zonal coordinates x are as indicated in Fig. 2; the meridional coordinate y is zero at the equator. Our model is based on the fully coupled (i.e., generating its own background state) version of the ZC model by van der Vaart et al. (2000), to which we add a simple representation of the Indian Ocean and a nonlinear convection feedback. A detailed description of the model with a linear atmosphere and an Indian Ocean extension is given in Wieners et al. (2017), so here, after a brief summary of the

linear atmosphere model (section 2a), we focus on the convection aspects (section 2b).

a. The linear atmosphere model

The Pacific component is the fully coupled pseudospectral ZC model of van der Vaart et al. (2000). The ocean dynamics is described by a linearized shallow-water reduced-gravity model on the equatorial β plane with a deep lower layer at rest and an active upper layer with horizontal velocities (u^r, v^r), separated by a thermocline at depth $H + h$ with $H = 200$ m (see Fig. 2). A mixed layer of depth $H_1 = 50$ m is embedded into the shallow-water layer
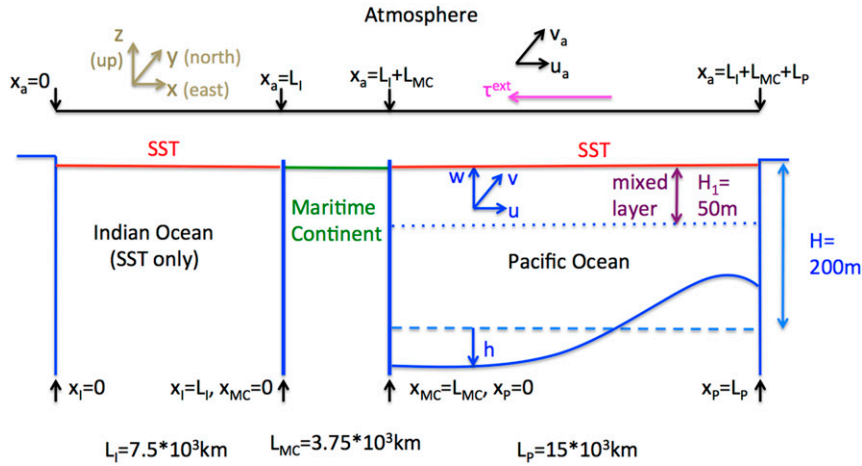
FIG. 2. Cross section along the equator ($y = 0$) of the model configuration with a Zebiak–Cane Pacific Ocean, an Indian Ocean with prescribed SST, and a Maritime Continent. Basins and continents are meridionally unbounded and coastlines are assumed strictly meridional.

to include the Ekman velocity (u^s, v^s). The total horizontal velocity in the mixed layer is given by $\mathbf{u}^1 = \mathbf{u}^r + \mathbf{u}^s$; vertical velocity is determined by mass conservation. Both for the Ekman velocity and the reduced-gravity model linear friction is assumed and they are forced by the wind stress $\boldsymbol{\tau} = (\tau^x_{\text{ext}} + \gamma_\tau u^a, \gamma_\tau v^a)$, where τ^x_{ext} is a weak externally generated easterly wind stress (thought of as being due to the Hadley circulation), (u^a, v^a) is the wind speed, and γ_τ is a constant (see Table 1) (i.e., the wind stress depends linearly on the wind speed). The sea surface temperature (SST) T is influenced by horizontal advection with velocity (u^1, v^1), upwelling of cold subsurface water, and radiative processes parameterized as linear Newtonian damping toward T_0.

The atmosphere of the original model is a linear Gill-type model (Gill 1980). The (dimensional) equations are given by

$$\epsilon^*_a u^a - \beta y v^a + \partial_{x_a}\phi = 0,$$
$$\beta y u^a + \partial_y\phi = 0, \quad \text{and}$$
$$\epsilon^*_a\phi + c^2_a(\partial_{x_a} u^a + \partial_y v^a) = -Q, \quad (1)$$

where x_a and y are the (dimensional) zonal and meridional coordinates as defined in Fig. 2, $\partial_x f$ is a shorthand for $\partial f/\partial x$, (u^a, v^a) is the (dimensional) wind velocity, and ϕ is the geopotential. The atmospheric damping parameter is denoted by ϵ^*_a; β is the local meridional derivative of the Coriolis parameter, and c_a is the atmospheric Kelvin wave phase speed. Term Q is a diabatic heating term. The atmospheric equations are diagnostic (i.e., contain no time derivatives) as the atmosphere is assumed to adjust instantaneously to the slowly varying SST field. In the linear atmosphere

model the heating is simply proportional to the deviation of the surface temperature T from a radiative equilibrium temperature T_0 [i.e., $Q = Q^T \equiv \alpha_T(T - T_0)$]. Several dimensional model parameters are given in Table 1; the other parameters are as in Wieners et al. (2017).

The Indian Ocean is modeled as in Wieners et al. (2017); that is, the ocean dynamics of the Indian Ocean are neglected and the Indian Ocean SST is represented as

$$T_I(x_I, y, t) = T_0 + \sum_{m=1}^{n_I} T^{0I}_m(x_I, y)A_m(t), \quad (2)$$

TABLE 1. Dimensional model parameters as used in the stability analysis in section 3a. In section 3a, $\gamma_\tau = 0.8\gamma^0_\tau$ was used. In section 3c, $\gamma_\tau = 0.8\gamma^0_\tau$ and $\gamma_c = 1.023c^2_a$ were used.

| Parameter	Meaning
$L_I = 7.5 \times 10^6$ m	Zonal length Indian Ocean
$L_{\text{MC}} = 3.75 \times 10^6$ m	Zonal length Maritime Continent
$L_P = 15 \times 10^6$ m	Zonal length Pacific Ocean
$L_a = L_I + L_{\text{MC}} + L_P$	Zonal length atmosphere
$\beta = 2.23 \times 10^{-11}$ m s^{-1}	Meridional derivative Coriolis parameter
$c_a = 30$ m s^{-1}	Atm Kelvin wave speed
$\epsilon^*_a = 0.22$ day^{-1}	Atm damping coefficient
$T_0 = 30°$C	Radiative equilibrium SST
$\Delta T = 1$ K	Scale of SST anomalies
$\tau_0 = 1.1 \times 10^{-2}$ N m^{-2}	Scale external wind stress τ_{ext}
$\alpha_y = 1500$ km	Meridional length scale T^{0I}_m, τ_{ext}, c_b, τ_{noi}
$\alpha_T = 3 \times 10^{-3}$ m^2 (K s^3)$^{-1}$	Surface heating–wind coupling
$\gamma^0_\tau = 1.6 \times 10^{-8}$ s^{-1}	Standard wind speed–wind stress coupling
$\gamma_c = 1.02c^2_a$	Convection feedback strength
$c^{0b} = -0.25L_a/c_a$	Background divergence strength
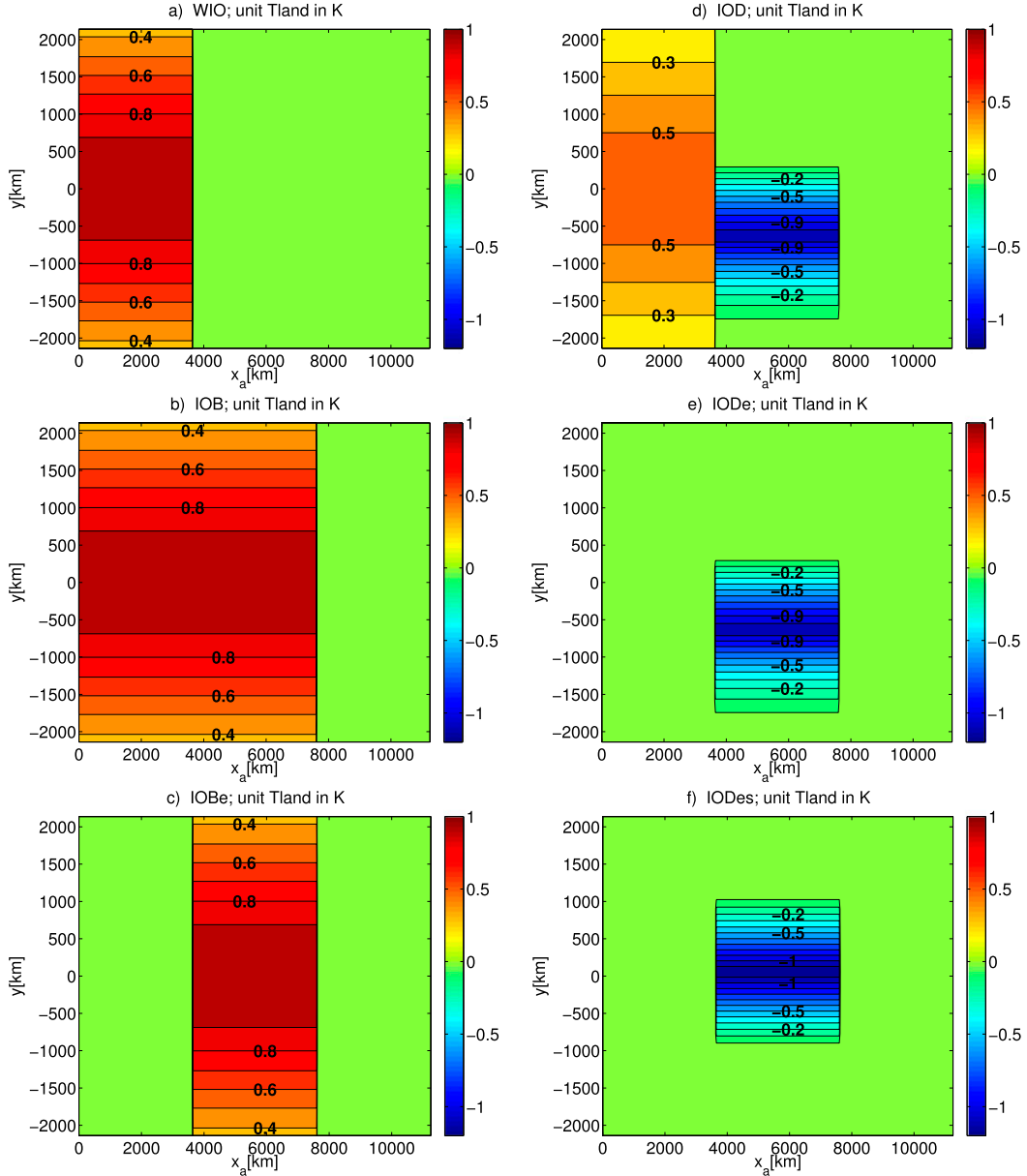
FIG. 3. The SST patterns in the Indian Ocean T_m^{0I} associated with $A_m = 1$ in (2). The patterns are associated with (a) the warm WIO, (b) the IOB, (c) the IOBe, (d) the IOD, (e) IODe, and (f) IODes. IOB is a combination of WIO and IOBe; IOD is a combination of $0.57 \times$ WIO and IODe. The zonal axis covers the Indian Ocean and Maritime Continent.

where T_m^{0I} is a prescribed spatial pattern of the Indian Ocean SST anomaly that can represent, for example, the IOD or IOB, and $A_m(t)$ is the time-dependent amplitude of this Indian Ocean SST anomaly that may depend on the state of the Pacific. The spatial patterns T_m^{0I} associated with $A_m(t) = 1$ are shown in Fig. 3. IOB is a combination of western Indian Ocean heating and eastern Indian Ocean heating (IOBe). IOD is a combination of $0.57 \times$ WIO and IODe; the latter represents

a cooling centered south of the equator. IOB and IOD are simplifications of observed patterns as shown in Fig. 4. IODes is like IODe but with the SST anomaly centered around the equator.

The evolution equation for $A(t)$ is of the form

$$\frac{dA}{dt} = a_0 \cos(\psi)(N - \overline{N}) + \frac{a_0}{\omega} \sin(\psi)\frac{dN}{dt} + a_d A + R(t),$$
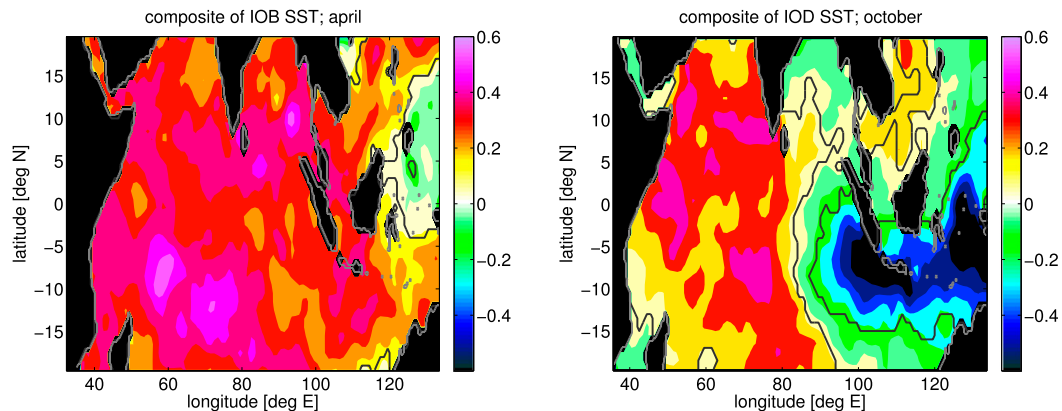$$(3)$$

FIG. 4. SST composite of (left) positive IOB years in April and (right) positive IOD years in October. Gray lines represent coastlines, and black lines encircle areas where the anomalies are significant at 90% confidence. Data are taken from HadISST (Met Office 2017; Rayner et al. 2003). Positive IOB (IOD) years are defined as years where the anomaly of IOB (February–April) [IOD (August–November)] exceeds 0.9 standard deviations.

where N is the El Niño index from Wieners et al. (2017) and $\overline{N}$ its equilibrium value ($N - \overline{N}$ is positive during El Niño). A noise term R is specified in section 3c below, and $a_d < 0$ is a damping constant. The coefficients a_0 and ψ control ϕ_{TI}, the phase difference between N and A (where subscript TI stands for temperature in the Indian Ocean). The normalization of the dN/dt term with $1/\omega$, where ω is the angular frequency of the ENSO mode, is inserted because sinusoidal oscillations N and $(dN/dt)/\omega$ have the same amplitude. For ENSO periods of around 3–4 yr and $\psi = 0$, $R = 0$, the amplitude A peaks a few months after N. There is no fixed relation between ϕ_{TI} and ψ because the ENSO period might change under the influence of the Indian Ocean. Note that for $R = 0$ and in equilibrium, $N = \overline{N}$ and $dN/dt = 0$; hence $A = 0$ (i.e., the

equilibrium solution is not influenced by the Indian Ocean). More details of the parameter choices in (3) will be provided in the sections 3a, 3b, and 3c below. The land surface temperature over the Maritime Continent is put to T_0.

b. The convection feedback

Similar to Zebiak and Cane (1987) and Zebiak (1986), we assume that convective heating can take place if there is converging horizontal wind and moisture because wind convergence near the ground leads to upward motion and—if sufficient moisture is present—condensation and latent heat release. Writing the wind divergence as $c(x_a, y) = \partial_{x_a} u^a + \partial_y v^a$, the convective heating Q^c can be parameterized as

$$Q^c(x_a, y) = \gamma_c m(x_a, y) \times \begin{cases} \{\mathcal{M}[-c(x_a, y) - c^b(x_a, y)]\}^\kappa & \text{if} & -c(x_a, y) - c^b(x_a, y) < C_0, \\ a_\kappa \{\mathcal{M}[-c(x_a, y) - c^b(x_a, y)]\}^{\bar{\kappa}} - b_\kappa & \text{else} \end{cases} \qquad (4)$$

where γ_c is a scaling parameter, m takes values between 0 and 1 and is a measure for moisture availability, c^b is a prescribed background divergence, and

$$\mathcal{M}(z) = \begin{cases} z & \text{if} & z > 0 \\ 0 & \text{if} & z \le 0 \end{cases};$$

that is, convergence leads to heating while divergence does not lead to cooling. The terms a_κ and b_κ are chosen such that Q^c is differentiable at $-c(x_a, y) - c^b(x_a, y) = C_0$. As opposed to Zebiak and Cane (1987), who have $\kappa = 1$, we use $\kappa = 1.5$. This supports strong heating anomalies at locations where the mean convergence is high, which is in

line with observations. To avoid numerical problems, we let the convective heating grow slower if the convection is very large, represented by setting $\bar{\kappa} = 0.5$. This is qualitatively in line with Gadgil et al. (1984), who suggest that convection does not increase if the SST is above a certain threshold [although others disagree (Roxy 2013)]. To avoid having very small-scale convective features, the divergence field is slightly smoothed (see appendix).

As we are interested in the effect of the Indian Ocean on ENSO, modified by convection over the Maritime Continent and over the eastern Indian Ocean, we let

$$m(x_a, y) = \begin{cases} (2x_a - L_I)/L_I & \text{if} & L_I/2 < x_a < L_I \\ 1 & \text{if} & L_I < x_a < L_I + L_{\text{MC}} \, ; \\ 0 & \text{else} \end{cases}$$

that is, $m(x_a, y) = 1$ over the Maritime Continent and linearly decreases to zero when moving westward over the eastern Indian Ocean. Although the western Pacific is part of the warm pool region, nonlinear convection there is neglected, as it would require careful tuning to implement it (the reason is the lack of a natural background convergence induced by the Hadley cell, which would compensate the mean wind divergence caused by the cold tongue SST). In addition, SST variability in the western Pacific is underestimated in our model, so the SST-induced convection anomalies can be expected to be small. Finally, the original model without convection and Indian Ocean generates reasonable ENSO variability in absence of western Pacific convection.

The background divergence c^b serves to include the convergence associated with the Hadley circulation, which is not explicitly included in our model and is given by

$$c^b(x_a, y) = c^{b0}(2x_a - L_I)/2L_I \times \exp[-(y^2/2\alpha_y^2)] \quad \text{for}$$
$$L_I/2 < x_a < L_I + L_{\text{MC}},$$

with $c^{b0} = -0.025 c_a/L_a$ and $c_a = 30 \, \text{m s}^{-1}$, the atmospheric Kelvin wave phase speed (see Table 1), and $\alpha_y = 1500$ km. The linear increase of c^b with x_a serves to compensate roughly the effect of the cold tongue cooling. Over the Pacific and western Indian Oceans c^b need not be specified as $m = 0$ there.

To test the robustness of our results, we repeated the simulations presented below in sections 3a and 3b with $\kappa \in \{1.0, 1.25, 1.75, 2.0\}$, $m = 1$ over the whole eastern Indian Ocean, and c_b zonally independent over the eastern Indian Ocean, the Maritime Continent, or both. In all cases, the results are qualitatively similar (not shown). In sections 3a and 3b, $-c(x_a, y) - c^b(x_a, y) < C_0$ in (4), so the results do not depend on C_0, provided it is not too small (i.e., $C_0 \gtrsim 0.89$). The results in section 3c do not change qualitatively when using $C_0 \in \{0.89, 1.25, 1.5, 2.0\}$.

The scaling parameter γ_c takes values in the order of c_a^2, as will be specified below. This is in agreement with Zebiak (1986), who finds that in the rotation-free case, $\gamma_c \lesssim c_a^2$ for $\kappa = 1$ (in Zebiak's notation: $\beta \equiv \gamma_c/c_a^2 \lesssim 1$). Owing to the smoothing of c and the presence of rotation, our model allows values a little larger than $\gamma_c = c_a^2$. In the convective case, the atmospheric continuity equation in (1) takes the form

$$\epsilon_a^* \phi + c_a^2(\partial_{x_a} u^a + \partial_y v^a) = -\alpha_T(T - T_0) - Q^c(x_a, y),$$

with $Q^c(x_a, y)$ from (4). As opposed to Zebiak and Cane (1987), we do not solve this equation iteratively but by adding c to the state vector. Details on the implementation of the convective feedback are provided in the appendix.

In the linear atmosphere model, the ocean–atmosphere coupling is characterized by $\alpha_T \gamma_\tau$, which determines how much wind stress is generated per surface heating anomaly. Only the product, but not the individual values of α_T and γ_τ, matter; hence $\tilde{\alpha}_T = \alpha_T \Delta T L_a/c_a^3$ (the nondimensionalized α_T) is arbitrarily put to unity (which amounts to scaling the dimensionless winds by $1/\tilde{\alpha}_T$). In the convective case, both wind stresses and winds (for the divergence) are needed; hence, α_T cannot be scaled arbitrarily but is taken from Zebiak (1986).[2]

c. Continuation

The extended Zebiak–Cane model from the previous section can be used both for transient simulations and stability analysis. Letting $\mathbf{z}$ be the state vector of all independent model variables (see the appendix), the model equations can be written in the form

$$\frac{d\mathbf{z}}{dt} = G(\mathbf{z}, p). \tag{5}$$

To determine how the equilibrium solutions $\bar{\mathbf{z}}$ of these equations change when one parameter p is varied, the pseudoarclength method of Keller (1977) is used. Adding a small perturbation $\tilde{\mathbf{z}}$ to $\bar{\mathbf{z}}$ (i.e., $\mathbf{z} = \bar{\mathbf{z}} + \tilde{\mathbf{z}}$) and linearizing (5) yields

$$\frac{d\tilde{\mathbf{z}}}{dt} = J\tilde{\mathbf{z}}, \tag{6}$$

where J is the Jacobian of G (i.e., $J_{kl} = \partial G_k/\partial z_l$). The solution of (6) is given by $\tilde{\mathbf{z}} = \exp(Jt)\tilde{\mathbf{z}}(0)$. Therefore, the equilibrium state $\bar{\mathbf{z}}$ is stable if all eigenvalues $\sigma = \sigma_r + i\sigma_i$ of J have negative real parts σ_r. Oscillatory modes of the system are characterized by a complex conjugate pair of eigenvectors and eigenvalues of J. In this study, we will be interested in the stability of the equilibrium solution with respect to the oscillatory mode associated with ENSO dynamics.

3. Results

In section 3a, linear stability analyses are first used to investigate the influence of convection on ENSO in the

---

[2] Zebiak and Cane (1987) has a typo; in their appendix α_T is a factor of 10 too large.

absence of Indian Ocean variability. Next, we address the issue whether cool WIO SST anomalies in presence of nonlinear convection can cause easterly wind anomalies over the western Pacific. In section 3b the effect of the dominant Indian Ocean modes of variability (IOD and IOB) on ENSO are investigated, again using linear stability analysis techniques. This same issue is addressed in section 3c using transient simulation, allowing for the effects of finite-amplitude perturbations (and noise).

a. Western Pacific easterlies caused by a cool western Indian Ocean

To compare situations with and without convection in the absence of Indian Ocean SST anomalies [all $T_m^{0I} = 0$ in (2)], we first consider changes in the Pacific background state and the ENSO mode when increasing γ_c from zero to $\gamma_c = 1.02c_a^2$. This increase of γ_c causes changes in the equilibrium state (see Fig. 5). The negative background divergence c^b in (4) over the MC leads to heating and enhanced convergence (Figs. 5c,d). The convergence-induced convective heating anomaly Q_c is divided by α_T to rescale it to an equivalent surface temperature, that is, the SST anomaly that would heat the atmosphere (in a Gill response) as much as Q_c. This heating in turn leads to stronger easterlies over the (western) Pacific (Figs. 5e,f), which induce more La Niña–like background conditions with a cooler eastern Pacific (Figs. 5a,b), a steeper thermocline (Figs. 5g,h), and more equatorial upwelling (Figs. 5i,j).

The stability of the background state is determined by solving the linear stability problem and determining the eigenvalue $\sigma_r \pm i\sigma_i$ of J in (6) with the largest real part. The corresponding eigenvector is referred to as the ENSO mode and the period of this mode is determined from $P = 2\pi/\sigma_i$. With increasing γ_c, the background state is destabilized as σ_r increases (see Table 2). The reason is that upwelling and thermocline feedbacks are strengthened as in the constant Indian Ocean warming experiments in Wieners et al. (2017). In Fig. 6, the anomalies associated with the oscillatory ENSO mode at $\gamma_c = 1.02c_a^2$ are shown. Note that stability analysis only yields the ENSO mode up to a normalization constant; both the real (Fig. 6, right) and imaginary (Fig. 6, left) parts of the eigenvector are plotted.

To characterize the effect of nonlinear convection on the winds over the Pacific, we define the following measures (cf. Fig. 7): ϕ_{TI} is the phase difference between A, the time-dependent amplitude of the Indian Ocean SST [see (2)], and the El Niño index N. It is measured in ENSO periods P and is positive if A peaks after N. Similarly, ϕ_{uTI} and ϕ_{uch} are the phase

difference between N and the zonal wind contribution at $(x_P = 0, y = 0)$ caused by SST heating Q^T and convergence-induced heating Q^c, respectively. They are positive if westerly winds are induced after El Niño. The amplitudes of the Indian Ocean SST and convection-induced zonal winds per unit A at $(x_P = 0, y = 0)$ are denoted by U_{TI} and U_{ch}, respectively. In the cases with zero IO (i.e., $A = 0$), U_{ch} cannot be normalized per unit A but is normalized by N. The amplitude of N is about 6 times as large as that of A.

ENSO-mode-related SST anomalies in the Pacific induce some relatively small anomalies in convective heating over the MC; their amplitude is $\approx 1/15$ of the amplitude of Pacific SST (cf. Figs. 6a,b with Figs. 6c,d). El Niño (La Niña) is followed by a divergence (convergence) anomaly above the equatorial MC (Figs. 6c,d), which leads to cooling (heating). The Q^c anomalies are of opposite sign to the SST anomalies in the eastern Pacific, which enhances the zonal temperature gradient over the Pacific and leads to stronger wind responses (Figs. 6e,f), which is qualitatively similar to enhancing the coupling strength α_T. The wind contribution induced by nonlinear convection is not exactly in phase with N but lags by about 1/8 ENSO periods ($\phi_{uch} = 0.12$ in Table 2, top), hence prolonging the westerlies (easterlies) associated with El Niño (La Niña). This may explain an increase in period seen in Table 2 (although changes in the background state can also affect the period).

To investigate the combined effect of the WIO anomalies and convection, we put $T^{0I} = T_{WIO}^{0I}$ in (2) and $\psi = 0°$, $R = 0$ in (3). As explained in section 2a, if the Indian Ocean SST obeys (3) with $R = 0$, it remains zero in equilibrium and hence does not affect the equilibrium solution. Hence, the background state for $\gamma_c = 1.02c_a^2$ in Fig. 5 remains unaltered throughout this and the following subsection. The linear stability result now leads to an eigenmode involving both the ENSO mode and anomalies in the amplitude A of the WIO. The above parameter choices lead to a peak in WIO SST about 3 months or 0.06 ENSO periods ($\phi_{TI} = 0.06$ in Table 2, top) after the peak in N, which agrees with observations. The amplitude of Indian Ocean SST (see Figs. 8c,d) is about 1/6 of the amplitude of N.

The heating parameter γ_c is next varied in order to determine whether it is possible to generate an easterly (westerly) wind response over the western Pacific in case of cool (warm) WIO SST anomalies. As can be seen in Figs. 8g–j, for $\gamma_c = 1.02c_a^2$ the zonal winds induced by Indian Ocean SST and nonlinear convection are of about equal magnitude and opposite sign. The value of γ_c for which the influence of the WIO variability on the
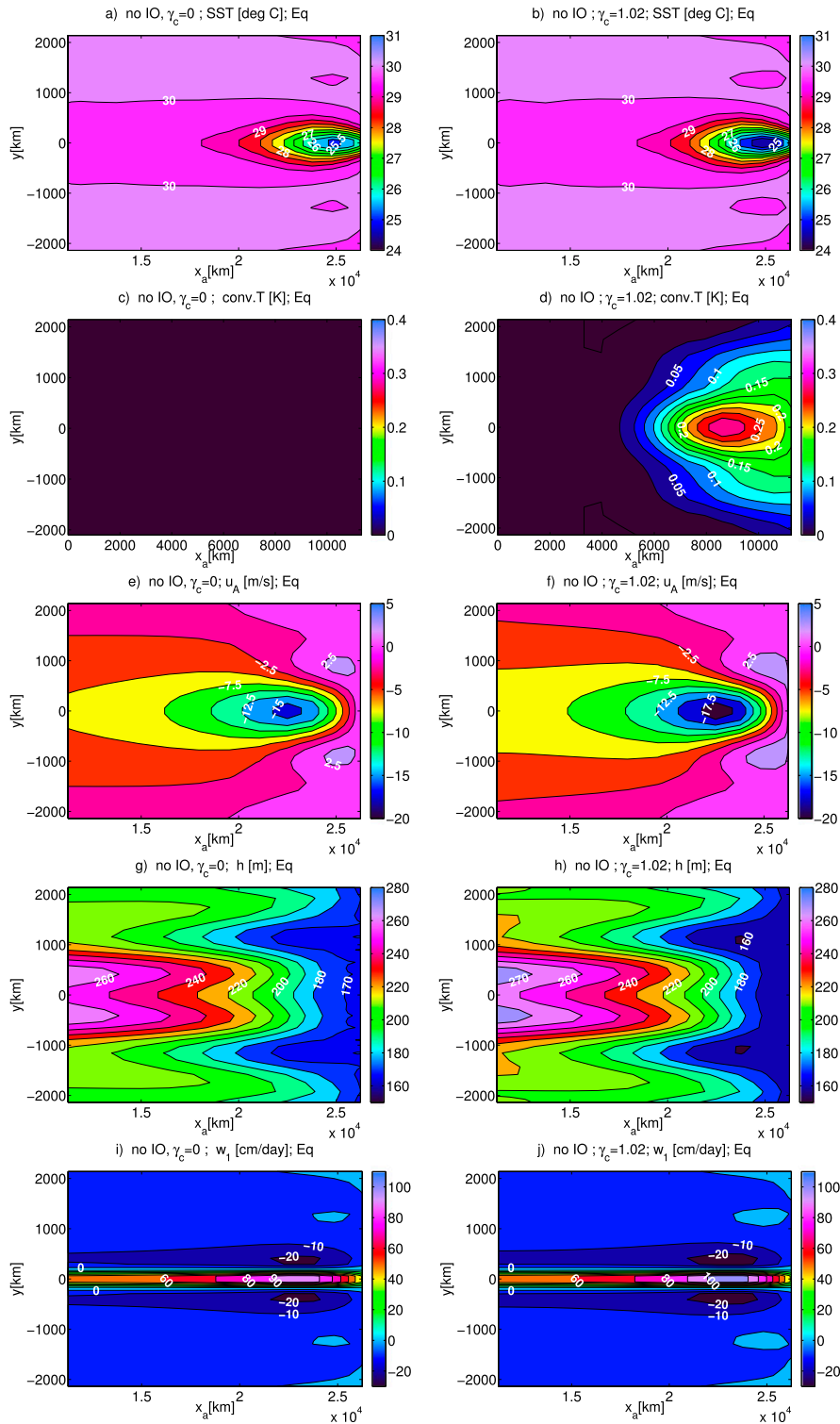
FIG. 5. The influence of convective heating on the equilibrium state. Equilibrium states are shown at (left) $\gamma_c = 0$ and (right) $\gamma_c = 1.02 c_a^2$. (a),(b) SST (in °C) over the Pacific; (c),(d) the convective heating (rescaled to equivalent surface temperatures in K) over the Indian Ocean and Maritime Continent, (e),(f) the zonal wind (in m s^{-1}) over the Pacific, (g),(h) the thermocline depth (in m) in the Pacific; (i),(j) the upwelling w_1 (in cm day^{-1}) in the Pacific mixed layer. The zonal coordinate x_a is as defined in Fig. 2.

TABLE 2. Results of the linear stability analysis for various IO configurations: no IO SST anomaly and no convection (zero IO, $\gamma_c = 0$), no IO SST anomaly but with convection (zero IO), warm western IO following El Niño (WIO), basinwide warming following El Niño (IOB), positive Indian Ocean dipole preceding El Niño (IOD), warm eastern half of IOB following El Niño (IOBe), cool eastern pole of IOD preceding El Niño (IODe), and cool eastern pole of IOD, shifted equatorward, preceding El Niño (IODes). The top of the table shows results for $\gamma_c = 1.02c_a^2$ (i.e., around the critical value), whereas the bottom of the table shows results for $\gamma_c = 0.90c_a^2$, well below the critical value. The measures denote the growth factor of the ENSO mode σ_r [positive (negative) if perturbations grow (decay)]; the period P; the phase difference between N and A measured in periods ϕ_{TI} (positive if A peaks after El Niño); the phase difference between N and the wind response over the western Pacific (in $x_P = 0$, $y = 0$) to Indian Ocean surface heating and convective heating in periods ϕ_{uTI} and ϕ_{uch}, respectively (positive if westerlies are induced after El Niño); the maximal zonal wind contribution in $x_P = 0$, $y = 0$ due to Indian Ocean SST and convection, normalized by A (U_{TI} and U_{ch}, respectively).

	Zero IO, $\gamma_c = 0$	Zero IO	WIO	IOB	IOD	IOBe	IODe	IODes
			Results for $\gamma_c = 1.02c_a^2$					
σ_r (yr^{-1})	−0.27	−0.08	−0.09	−0.88	0.50	−0.87	0.52	1.16
P (yr)	3.8	4.2	4.1	2.6	4.4	2.7	4.5	8.2
ϕ_{TI} (P)	—	—	0.06	0.11	−0.08	0.11	−0.08	−0.03
ϕ_{uTI} (P)	—	—	−0.44	−0.39	0.42	−0.39	−0.08	−0.03
ϕ_{uch} (P)	—	0.12	0.08	−0.40	−0.06	−0.39	−0.05	−0.03
U_{TI} (m s^{-1})	—	—	2.68	6.71	0.08	4.03	1.44	1.67
U_{ch} (m s^{-1})	—	0.11[a]	3.18	1.85	4.55	4.41	3.14	6.95
			Results for $\gamma_c = 0.90c_a^2$					
σ_r (yr^{-1})	−0.27	−0.14	−0.26	−0.80	0.02	−0.62	0.14	0.23
P (yr)	3.8	4.0	3.6	2.8	3.9	3.0	4.0	4.0
ϕ_{TI} (P)	—	—	0.07	0.11	−0.08	0.10	−0.10	−0.09
ϕ_{uTI} (P)	—	—	−0.43	−0.39	0.39	−0.40	−0.10	−0.09
ϕ_{uch} (P)	—	0.14	0.08	−0.40	−0.08	−0.41	−0.06	−0.06
U_{TI} (m s^{-1})	—	—	2.68	6.71	0.08	4.03	1.44	1.67
U_{ch} (m s^{-1})	—	0.03[a]	1.21	0.62	1.49	1.59	0.95	1.38

[a] In the simulations with zero IO, $A = 0$; hence normalization by A is not possible, and normalization was performed with the El Niño index N. Typically, N is around 6 times as large as A, which means that U_{ch} is relatively small, but not negligible, in the zero IO case.

wind over the Pacific becomes zero is referred to as $\gamma_{c,\text{crit}}$ below. Because of the small but nonzero influence of the eastern Pacific on MC convection, one cannot determine the value of $\gamma_{c,\text{crit}}$ exactly. For the case $\psi = 0$ presented here, U_{ch} is slightly larger than U_{TI} because the contributions to convective heating induced by ENSO and the WIO are roughly in phase; if one chooses $\psi = 180°$, U_{ch} is slightly smaller than U_{TI} (not shown). As one would expect, given the near-cancellation of the WIO-induced winds, both the spatial SST patterns and the period and growth factor of the ENSO mode (see Figs. 6a,b and 8a,b) change very little when adding WIO variability at $\gamma_c = \gamma_{c,\text{crit}}$.

The U_{ch} becomes larger by a factor of about 5 when including the WIO (see Table 2, top, bearing in mind that in the WIO case U_{ch} was normalized with A and in the zero IO case with N, whose amplitude is ≈6 times as large as that of A). This is in line with Watanabe and Jin (2002) and can be explained by the relatively large distance between the MC and the east Pacific and also the fact that the Gill response is more zonally extended to the east of an SST anomaly than to the west; that is, compared to Indian Ocean SST anomalies, eastern Pacific SST anomalies have relatively little effect on the divergence over the

MC. Figures 8g–j also show that the winds due to WIO SST and convergence-induced heating have exactly the same spatial pattern; this is a general feature of the Gill response to the east of a surface heating anomaly (Indian Ocean and MC). Figures 8e,f show the convergence-induced heating (rescaled to equivalent temperature), which is positive when the WIO is cool.

If $\gamma_c < \gamma_{c,\text{crit}}$, a cool (warm) WIO anomaly generates a westerly (easterly) contribution to the wind over the Pacific. As A peaks shortly after El Niño ($\phi_{TI} > 0$), these winds counteract the winds associated with ENSO and dampen the ENSO mode (Table 2, bottom). If $\gamma_c > \gamma_{c,\text{crit}}$, a cool (warm) WIO leads to easterlies (westerlies) and the growth factor of ENSO increases. For example, for $\gamma_c = 1.025c_a^2$ one obtains $\sigma_r = +0.04 \text{ yr}^{-1}$, as opposed to -0.09 yr^{-1} for $\gamma_c = 1.02c_a^2$, and the amplitudes U_{TI} and U_{ch} of the zonal wind contributions induced by Indian Ocean SST and convection, respectively, take the values $U_{TI} = 2.68 \text{ m s}^{-1}$, $U_{ch} = 4.10 \text{ m s}^{-1}$. These results suggest that it is possible, at least in principle, through convection above the MC, that a cool (warm) WIO leads to easterlies (westerlies), as suggested in Wieners et al. (2016). However, it is not clear whether such high values of γ_c are realistic.
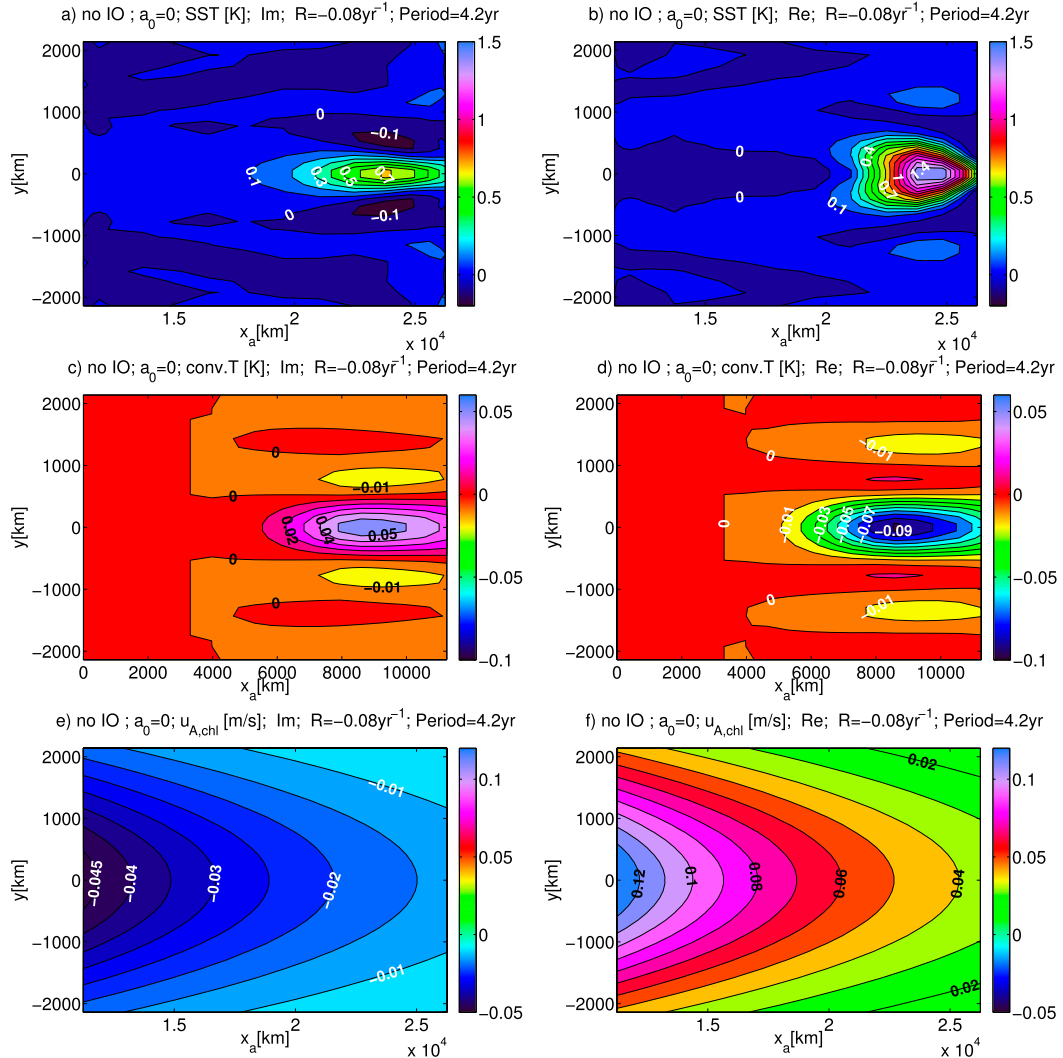
FIG. 6. The ENSO mode in the zero IO case at $\gamma_c = 1.02c_a^2$. The (left) imaginary and (right) real parts of the eigenvector; the imaginary part is leading by 1/4 period. (a),(b) The SST anomalies (in K) in the Pacific, (c),(d) the convective heating anomalies (rescaled to the equivalent surface temperature in K) over the IO and Maritime Continent, (e),(f) the contribution of the convective heating to the zonal wind over the Pacific (in m s^{-1}). As this mode is an eigenvector of J in (6), it can only be computed up to an overall scaling factor. The zonal coordinate x_a is defined in Fig. 2.

b. Wind effect of IOB and IOD

The two dominant modes of Indian Ocean variability are the IOB and IOD, and their effects on convection and Pacific winds are investigated in this subsection. For the IOB, $T^{0I} = T_{\text{IOB}}^{0I}$ (see Fig. 3) and $\psi = 0$ is chosen; that is, the Indian Ocean warms over its full zonal width a few months after El Niño. The IOD is modeled with $T^{0I} = T_{\text{IOD}}^{0I}$ and $\psi = 60°$; that is, a positive IOD occurs a few months before El Niño. For a better understanding of the contribution of the EIO, the eastern half of the IOB (IOBe) and eastern pole of the IOD (IODe) are also included, with $\psi = 0$ and $\psi = 60°$, respectively.

IODes is like IODe but with the SST anomaly shifted toward the equator. For all these cases, R, a_d, and a_0 are as in section 3a and $\gamma_c = 1.02c_a^2$. As $\gamma_c = 1.02c_a^2$ might be an unrealistically high value, the experiments are repeated with $\gamma_c = 0.9c_a^2$.

Table 2 summarizes the results for the new cases considered. The spatial SST and thermocline patterns of the ENSO mode (not shown) do not differ strongly from the WIO case (as shown in Figs. 8a,b and 8e,f). The convergence-induced heating Q^c, taken at the phase where A is maximal, is shown in Fig. 9 for $\gamma_c = 1.02c_a^2$ and all cases considered. Note that maximal A coincides with a warm WIO, warm IOB, warm IOBe, positive IOD, cool
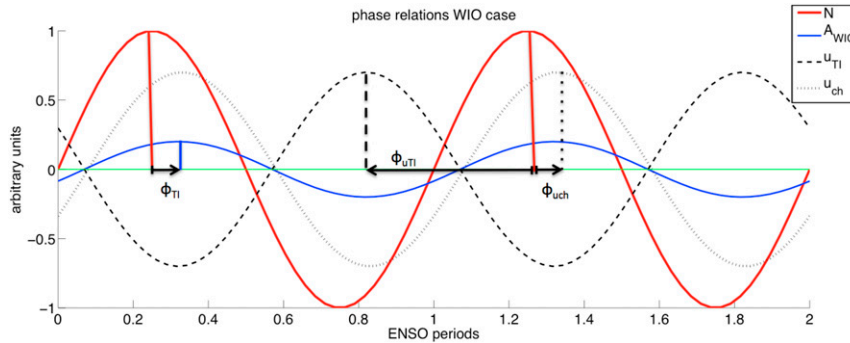
FIG. 7. Illustration of the phase relations in the WIO case. The solid red line denotes the El Niño index N, the solid blue line the amplitude A of the Indian Ocean SST pattern (here, WIO), and the black dashed and dotted lines the zonal wind contribution in the western Pacific ($x_P = 0$, $y = 0$) induced by Indian Ocean SST u_{TI} and convective heating u_{ch}, respectively. The phase difference ϕ_{TI} between N and A is positive if A peaks later than N. The phase differences ϕ_{uTI} and ϕ_{uch} between N and the zonal winds induced by the Indian Ocean SST and convective heating, respectively, are positive if N is followed by westerlies. All phase differences are measured in ENSO periods.

IODe, and cool-shifted IOD for Figs. 9a–f, respectively (see also Fig. 3). The fields are normalized by $|A|$, the amplitude of A.

While a warm WIO (Fig. 9a) is associated with a cool Q^c anomaly reaching $-1.1K$, a warm IOBe (Fig. 9c) yields a warm anomaly of 2.6 K. For the full IOB, the effects of WIO and IOBe partially cancel and Q^c only reaches 1.6 K (Fig. 9b). This partial cancellation explains the relatively low value of $U_{ch} = 1.85$ m s^{-1} in Table 2, top. In contrast, $U_{TI} = 6.71$ m s^{-1} is large for the IOB because a large area is covered by warm SSTs. The two wind contributions are nearly in phase ($\phi_{uTI} \approx \phi_{uch}$), and the effect of the IOB is to induce easterlies (westerlies) during El Niño (La Niña), which damp the ENSO mode ($\sigma_r = -0.88$ yr^{-1}; i.e., smaller than for the zero IO case) and shorten the period, as the Indian Ocean–induced winds peak slightly after ENSO and facilitate the transition to the other ENSO phase.

A cool IODe (Fig. 9e) leads to a decrease in Q^c, up to -3.3 K. In the full IOD (Fig. 9d), the effects of WIO and IODe are of the same sign, yielding an anomaly of -3.8 K. (Recall that $T_{IOD}^{0I} = T_{IODe}^{0I} + T_{WIO}^{0I} \times 0.57$.) Fig. 9f illustrates that the impact of the IODe on Q^c would be ≈ 1.5 times higher if IODe were located on the equator. Since the Gill response to IOD is very small ($U_{TI} = 0.08$ m s^{-1}) due to cancellation of the contributions of the two poles, the wind effect above the Pacific is mainly due to the convergence-induced convection effect. The IOD leads to westerlies (easterlies) just before El Niño (La Niña), which increases the growth factor to $\sigma_r = +0.52$ yr^{-1}. The period is not much affected because the effect of IOD-induced winds on thermocline and SST lags a few months behind the winds themselves and thus peaks almost simultaneously with N.

So the switch to La Niña (El Niño) is neither accelerated nor delayed. Since Annamalai et al. (2010) suggest that the marginal seas in the MC, whose SST develops in phase with the IODe during an IOD event, also play an important role, we repeated the IOD experiment with IODe shifted eastward by $L_I/4$. The result (not shown) is qualitatively similar to the IOD experiment, but the convective winds are stronger ($U_{ch} = 8.5$ m s^{-1}).

Although for the smaller value $\gamma_c = 0.9c_a^2$ the winds induced by the WIO are dominated by the Gill response ($U_{ch} < U_{TI}$ in Table 2, bottom), it still holds that the IOB dampens ENSO and is dominated by Gill response, whereas the IOD destabilizes the ENSO mode and its winds are induced by convergence-induced heating anomalies to which both the WIO and IODe contribute.

In the presence of IOB (IOD) influence, a higher (lower) coupling constant α_T is needed to obtain a self-sustained ENSO oscillation (i.e., the critical coupling associated with the Hopf bifurcation is shifted). The impact of Indian Ocean–induced winds on the Hopf bifurcation is discussed in Wieners et al. (2017).

c. Transient simulation

A linear stability analysis as performed in the previous subsections only applies to the evolution of infinitesimal perturbations of the equilibrium state. To include finite-amplitude anomalies and noise, we performed a set of simulations of 150 years each. In each of them, the seasonal cycle is neglected.

The most realistic simulation, referred to as the reference (REF) case, includes both the dominant Indian Ocean modes IOB and IOD. Hence, (2) takes the form
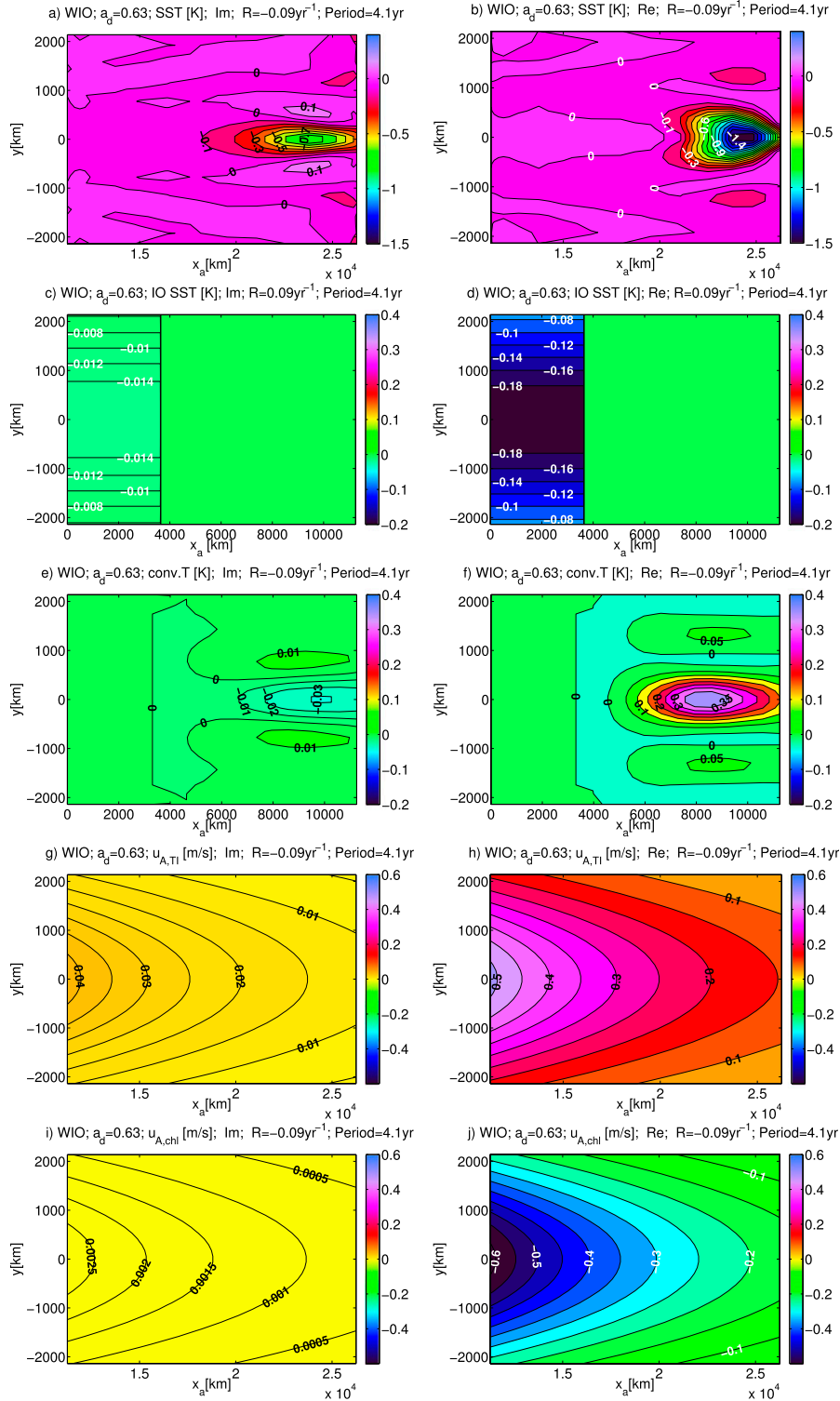
FIG. 8. The ENSO mode in the WIO case. The (left) imaginary and (right) real parts of the eigenvector; the imaginary part is leading by 1/4 period. (a),(b) The SST (in K) in the Pacific, (c),(d) the IO SST (in K), (e),(f) the convective heating (rescaled to the equivalent surface temperature in K) over the IO and Maritime Continent, and (g),(h) the contribution of the IO SST to the zonal wind over the Pacific (in m s^{-1}); (i),(j) as in (g),(h), but for convective heating instead of IO SST. The zonal coordinate x_a is defined in Fig. 2.
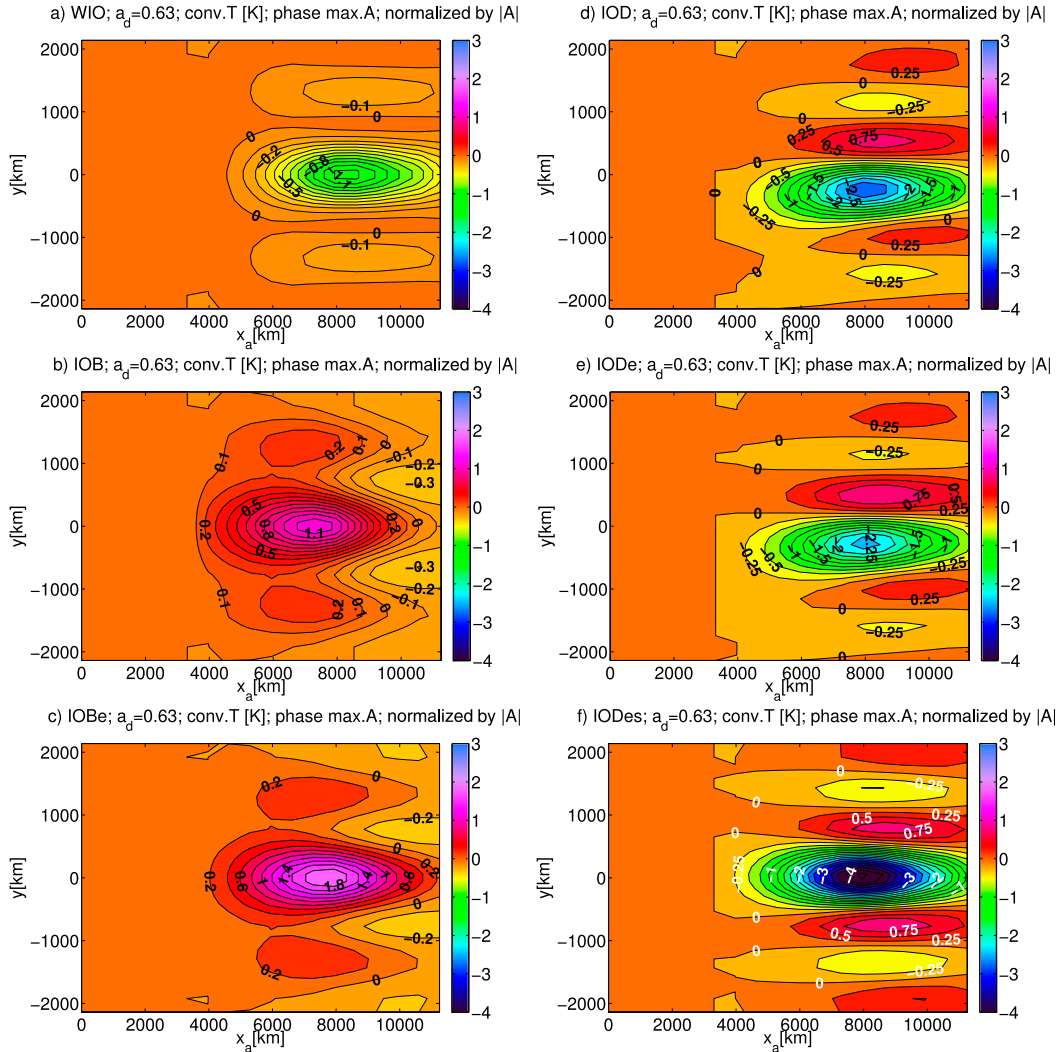
FIG. 9. The convective heating (rescaled to equivalent temperature) associated with the T_m^{0I} from Fig. 3, for $\gamma_c = 1.02c_a^2$. The patterns shown here are derived from the ENSO mode of a continuation experiment and show the convective heating in the moment of the ENSO cycle where A is maximal. The fields are normalized by $|A|$, the amplitude of A. The plots are for T_m^{0I} being (a) WIO, (b) IOB, (c) IOBe, (d) IOD, (e) IODe, and (f) IODes.

$$T_I(x_I, y, t) = T_0 + T_{IOD}^{0I}(x_I, y)A_{IOD}(t) + T_{IOB}^{0I}(x_I, y)A_{IOB}(t),$$
(7)

and T_{IOD}^{0I} and T_{IOB}^{0I} are as in Fig. 3. The evolution of the A is as in (3) with a noise term $R(t) = \eta r(t)$. Here η is a scaling factor and $r(t)$ is pink noise; that is, at time step t_i, $r(t_i) = b_1 r(t_{i-1}) + b_2 s(t_i)$, where the $s(t_i)$ are normally distributed random numbers, and b_1 and b_2 are chosen such that r has a $1/e$-folding time of 2 months (i.e., rather long intraseasonal time scales) and unit standard deviation. In addition, noise is added to the zonal wind stress in the Pacific, with a spatial pattern

$$\tau_{noi}^x = \frac{\eta_\tau}{2}[1 - \cos(2\pi x_P/L_P)]\exp(-y^2/2\alpha_y^2),$$

where $\eta_\tau = 5.5 \times 10^{-3}\,\mathrm{N\,m^{-2}}$ and the $r(t)$ for the IOD, IOB, and τ_{noi}^x are uncorrelated. The convection scaling parameter γ_c is put to $1.023c_a^2$ (i.e., slightly more than $1.020c_a^2$) so that a cool WIO should lead to easterlies over the western Pacific. The coupling parameter is put to $\gamma_\tau = 0.80\gamma_\tau^0$ (see section 2a; Table 1), such that in absence of Indian Ocean influence ($A = 0$) the ENSO mode would be slightly damped.

A list of the parameter choices in the reference simulation is provided in Table 3, while the parameter changes with respect to REF for the sensitivity studies are given in Table 4. The parameters for the Indian Ocean modes and Pacific noise in REF are chosen such that the standard deviations of and correlations between the El Niño index and the IOB and IOD

TABLE 3. Settings for time integrations for REF. Other parameters are as in Table 1. Further explanations are given in section 3c.

List of parameters in REF	
Parameter	Value
γ_τ	$0.8\gamma_\tau^0$
γ_c	$1.023c_a^2$
$a_{0,\mathrm{IOD}}$	$0.26\ \mathrm{yr}^{-1}$
$a_{d,\mathrm{IOD}}$	$-3.78\ \mathrm{yr}^{-1}$
ψ_{IOD}	$60°$
η_{IOD}	$1.01\ \mathrm{yr}^{-1}$
η_τ	$0.55\ \mathrm{N\,m}^{-2}$
$a_{0,\mathrm{IOB}}$	$0.84\ \mathrm{yr}^{-1}$
$a_{d,\mathrm{IOB}}$	$-3.78\ \mathrm{yr}^{-1}$
ψ_{IOB}	$0°$
η_{IOB}	$1.05\ \mathrm{yr}^{-1}$

TABLE 4. Summary of the sensitivity experiments by specifying the changes with respect to REF.

Name	Changes with respect to REF (Table 3)
REF	No change
IO*0	$T_{\mathrm{IOD}}^{0I} \to T_{\mathrm{IOD}}^{0I} \times 0,\ T_{\mathrm{IOB}}^{0I} \to T_{\mathrm{IOB}}^{0I} \times 0$
IOD*0	$T_{\mathrm{IOD}}^{0I} \to T_{\mathrm{IOD}}^{0I} \times 0$
IOD*0.5	$T_{\mathrm{IOD}}^{0I} \to T_{\mathrm{IOD}}^{0I} \times 0.5$
IOD*2	$T_{\mathrm{IOD}}^{0I} \to T_{\mathrm{IOD}}^{0I} \times 2$
IOB*0	$T_{\mathrm{IOB}}^{0I} \to T_{\mathrm{IOB}}^{0I} \times 0$
IOB*0.5	$T_{\mathrm{IOB}}^{0I} \to T_{\mathrm{IOB}}^{0I} \times 0.5$
IOB*2	$T_{\mathrm{IOB}}^{0I} \to T_{\mathrm{IOB}}^{0I} \times 2$
IODnoi	$a_{0,\mathrm{IOD}} = 0; a_{d,\mathrm{IOD}} = -1.39\,\mathrm{yr}^{-1}; \eta_{\mathrm{IOD}} = 0.76\,\mathrm{yr}^{-1}$

indices roughly resemble observed values. Using the HadISST data at 1° resolution (Met Office 2017; Rayner et al. 2003), we calculated standard deviations $\sigma(\mathrm{Niño\text{-}3.4}) \approx 1\,\mathrm{K}$ in boreal winter, $\sigma(\mathrm{IOD_{obs}}) \approx 0.35\,\mathrm{K}$ (autumn), and $\sigma(\mathrm{IOB_{obs}}) \approx 0.25\,\mathrm{K}$ (spring). Here $\mathrm{IOD_{obs}}$ is the standard IOD index, that is, the SST anomaly (in K) averaged over $10°\mathrm{S}-10°\mathrm{N}, 50°-70°\mathrm{E}$ minus the SST anomaly over $10°\mathrm{S}-0°, 90°-110°\mathrm{E}$ (Saji et al. 1999). The $\mathrm{IOB_{obs}}$ is the SST anomaly averaged over $20°\mathrm{S}-20°\mathrm{N}, 40°-100°\mathrm{E}$ (Saji et al. 2006). The correlations between these indices are given by $\mathrm{corr}(\mathrm{Niño\text{-}3.4}, \mathrm{IOD_{obs}}) \approx 0.6$ for Niño-3.4 in boreal winter and $\mathrm{IOD_{obs}}$ in the previous boreal autumn and $\mathrm{corr}(\mathrm{Niño\text{-}3.4}, \mathrm{IOB_{obs}}) \approx 0.85$ for Niño-3.4 in boreal winter and $\mathrm{IOB_{obs}}$ in the following spring.

Here we approximate Niño-3.4 by N and define model IOD and IOB indices as $A_{\mathrm{IOD}} \times [T_{\mathrm{IOD}}^{0I}(\mathbf{x}_{\mathrm{WIO}}) - T_{\mathrm{IOD}}^{0I}(\mathbf{x}_{\mathrm{IODe}})]$ and $A_{\mathrm{IOB}} \times T_{\mathrm{IOB}}^{0I}(\mathbf{x}_{\mathrm{IOB}})$, where $\mathbf{x}_{\mathrm{IODe}}, \mathbf{x}_{\mathrm{WIO}},$ and $\mathbf{x}_{\mathrm{IOB}}$ are the positions where the IODe, WIO, and IOB have their strongest SST signal. Plots of the modeled lag correlations (between IOD and N, IOB and N, and the autocorrelation of N) for the REF case are provided in Fig. 10a. Values of the correlations at various local maxima and minima with the corresponding lags, as well as the standard deviations of the indices, are given in Table 5. Note that lags are defined as positive if N is leading. The value of the first peak at nonzero lag in the autocorrelation of N may serve to characterize how strongly periodic the ENSO cycle is, and the lag at which this peak occurs serves as proxy for the ENSO period.

As can be seen in Table 5, the standard deviations and correlations at small lags of these quantities in the REF case agree reasonably well with observations; however, $\mathrm{std}(N)$ is overestimated by a factor of 1.5 and the ENSO period is shorter than observed. The lags of $\mathrm{corr}(N, \mathrm{IOD})$ (for IOD events occurring a few months

before ENSO) and $\mathrm{corr}(N, \mathrm{IOB})$ are also a bit shorter than in observations but take reasonable values despite the lack of a seasonal cycle. As in observations, $\mathrm{corr}(N, \mathrm{IOD})$ has a minimum at -15 months lag, but the cause for this is different from reality. In observations, a cool WIO or negative IOD in autumn tend to be followed by El Niño after 15 months, without necessarily a La Niña occurring in between. In the simulations presented here, the negative IOD is first followed by La Niña and, half a (short) ENSO period later, by El Niño. In reality, only some negative IOD events are followed by La Niña in the same year (or rather, they co-occur with the developing La Niña; it is hard to disentangle cause and consequences from observations alone), but even a negative IOD occurring independently from La Niña can be followed by El Niño after 15 months. We hypothesize that this can be explained by the influence of the seasonal cycle, which is lacking in our simulations. In observations, a negative IOD occurring independently of ENSO may cause easterlies over the western Pacific, but this happens typically in boreal autumn (the IOD season), that is, too late in the year to induce a major La Niña [although IOD events starting early in the season can reenforce ENSO events (Luo et al. 2010)]. However, warm water is pushed to Indonesia and reloads the warm water volume, thus facilitating El Niño development in the next year.

Next, we decouple the Indian Ocean by multiplying T_{IOB}^{0I} and T_{IOD}^{0I} by zero (the IO*0 case). This leads to an increase in both $\sigma(N)$ and the ENSO period by a factor of ≈ 2 (see Table 5), so the net effect of the Indian Ocean is to damp the ENSO mode and shorten its period, which agrees with previous studies (Frauen and Dommenget 2012; Kajtar et al. 2017). To understand in more detail how the IOD and IOB act on ENSO, a set of sensitivity studies was performed by increasing or reducing T_{IOB}^{0I} and T_{IOD}^{0I}, that is, the magnitude of their spatial patterns. The equation for A (and hence the balance between ENSO and noise influence on the Indian Ocean)
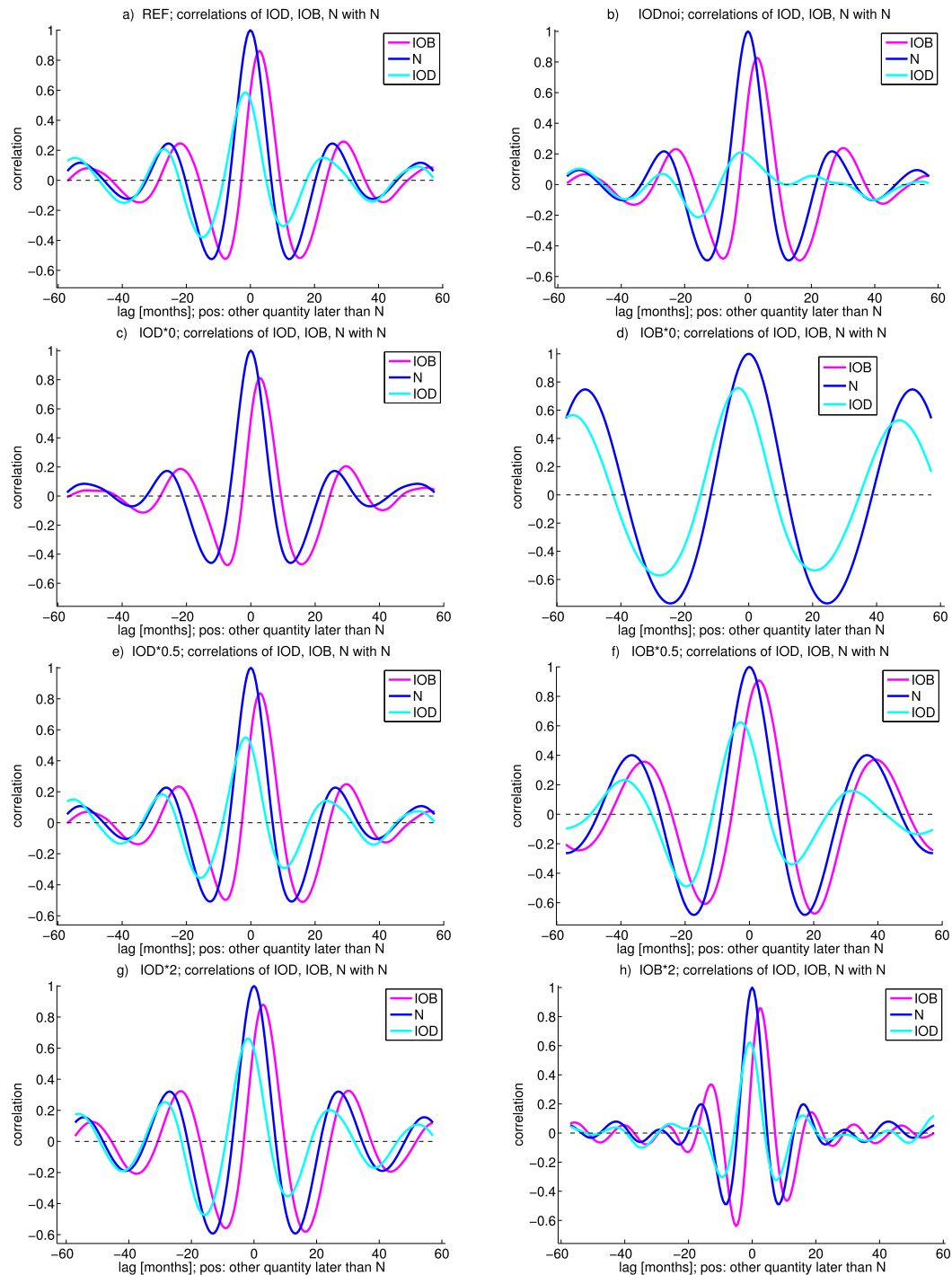
FIG. 10. Lagged correlations between IOB and the El Niño index N (purple), IOD and N (light blue), and N with itself (dark blue). Lags are in months and positive if N is taken at an earlier time than the other quantity.

remains unchanged. What is directly changed in this way is the influence of the IOD or IOB on ENSO (and not vice versa). The numerical simulations are summarized in Table 4 and the results are provided in Table 5 and Fig. 10. It can be seen that the IOB has a strong damping

effect on ENSO and shortens its period, while the IOD has little effect on the period but increases ENSO variability. The case IOB*2 is an exception because here the ENSO period is so much reduced that the peak impact of the IOB-induced easterlies (westerlies) occurs not

TABLE 5. Results of the time integration sensitivity experiments. The labels of the simulations are explained in Table 4. The measures provided here are the standard deviations of the El Niño index N and the model IOB and IOD indices (see section 3c); the correlation between N and IOB at its global maximum and the corresponding lag (positive if N is leading); the correlation between N and IOD at its global maximum with its lag (positive it N is leading); the correlation between N and IOD at its local minimum at lags of around $-1/2$ ENSO period, the value of this lag; the autocorrelation of N at the local maximum at a lag around one ENSO period, and the value of this lag (a proxy for the period). For IOB*2, 2 times the lag of the first minimum was used instead because there is no clear maximum (see Fig. 10h). All lags are given in months.

	REF	IO*0	IOD*0	IOD*0.5	IOD*2	IOB*0	IOB*0.5	IOB*2	IODnoi
$\sigma(N)$ (K)	1.58	2.99	1.46	1.57	1.84	3.59	2.03	1.86	1.53
σ(IOB) (K)	0.30	—	0.26	0.28	0.33	—	0.20	0.55	0.27
σ(IOD) (K)	0.32	—	—	0.16	0.68	0.40	0.33	0.34	0.36
corr(N, IOB)	0.86	—	0.81	0.83	0.88	—	0.90	0.86	0.83
lag(N, IOB)	2.3	—	2.6	2.5	2.3	—	2.9	2.5	2.6
corr(N, IOD)	0.58	—	—	0.55	0.66	0.75	0.62	0.62	0.21
lag(N, IOD)	−1.7	—	—	−1.7	−2.0	−3.2	−2.6	−0.6	−2.1
corr(N, IOD)	−0.38	—	—	−0.36	−0.47	−0.57	−0.50	−0.30	−0.21
lag(N, IOD)	−14.9	—	—	−15.6	−15.8	−28.0	−19.7	−9.1	−15.7
corr(N, N)	0.25	0.73	0.17	0.23	0.32	0.75	0.40	0.20	0.22
lag(N, N)	25.7	52.0	26.3	26.3	26.8	51.2	36.6	16.0	26.5

shortly after El Niño (La Niña) but almost during the zero crossing of N (the impact on SST lags a few months behind the winds), so the damping becomes less efficient. However, the noise contribution to IOB tends to enhance the variability both of IOB itself and ENSO, and this effect is amplified by doubling T_{IOB}^{0I}. In general, our findings agree with those in section 3b and suggest that the IOB has a larger influence than the IOD on the spectral properties of ENSO.

Increasing the influence of the IOD and decreasing that of the IOB both lead to stronger corr(N, IOB), corr(N, IOD), and corr(N, N). This is because both lead to a larger ENSO amplitude; hence, the impact of noise on IOD, IOB, and the Pacific dynamics becomes relatively smaller, and correlations grow.

As mentioned, the IOB seems to have a stronger effect on ENSO period and standard deviation than the IOD, despite the fact that both have similar standard deviations in REF. One important reason is that the wind response per unit IOB is about 4.5 times as strong as the response per unit IOD. This was estimated by performing a partial regression of the total wind contribution due to Indian Ocean SST and convective heating onto N, IOB, and IOD (not shown). The main reason for this increase is the large Gill response to IOB forcing (see Table 2), while the partial regression of $u_{\mathrm{ch}}(x = L_I + L_{\mathrm{MC}}, y = 0)$ onto N, IOB, and IOD yields 0.04, −0.44, and 0.36 m s^{-1} K^{-1}, respectively. Hence, IOD and IOB have a similar impact on convergence-induced convection. As in section 3a, the impact by ENSO on convection is smaller than that of the IO but not negligible.

Another potentially important factor is the timing of Indian Ocean–induced wind anomalies with respect to the ENSO cycle. The results in Wieners et al. (2017) suggest that Indian Ocean–induced easterlies peaking slightly before El Niño (La Niña), that is, when N is maximal (minimal), are optimal for reducing (increasing) ENSO variability (the amplitude effect). Likewise, Indian Ocean–induced easterlies peaking slightly before the sign switch of N, that is, the transition from La Niña to El Niño (from El Niño to La Niña), are optimal for increasing (shortening) the ENSO period (the period effect). The latter can explain why the IOD has so little influence on the period: It peaks slightly before El Niño. However, the timing of IOD influence is almost optimal for enlarging the ENSO amplitude. To be precise, the growth factor becomes largest if $\psi \approx 73°$ in (3), which corresponds to $\phi_{\mathrm{TI}} \approx -0.11$ in Table 2 (not shown). Note that Luo et al. (2010) also find that the impact of the IOD on the ENSO amplitude is largest relatively early in the season, although their result is also influenced by the seasonal cycle.

A third factor is the regularity with which the Indian Ocean influence affects ENSO. We hypothesize that the effect of the IOD on the spectral properties of ENSO is reduced by the fact that the IOD is less strongly correlated to N; that is, its influence does not occur as regularly within the ENSO cycle as that of the IOB. To test this hypothesis, one additional simulation is performed, in which the IOD is entirely driven by the noise and not affected by ENSO at all [$a_{0,\mathrm{IOD}} = 0$ in (3)]. In this simulation, labeled IODnoi, η_{IOD} and $a_{d,\mathrm{IOD}}$ are chosen such that the standard deviation of IOD is similar to that in REF and the $1/e$-folding time of IOD is about a year. In the IODnoi case, $\sigma(N)$ is larger than in the IOD*0 case but lower than for REF. Also, corr(N, IOD) at small negative lags is smaller for IODnoi than for REF (cf. Table 5). The positive corr(N, IOD) at small negative lags in IODnoi suggests

that a positive (negative) IOD is likely to be followed by El Niño (La Niña), which is to be expected because a positive (negative) IOD leads to westerlies (easterlies) over the Pacific. On the other hand, compared to the IODnoi case, the equation for A_{IOD} in REF also tends to let the IOD peak shortly before N even if the influence of the IOD on ENSO were absent. The combination of these two effects—the influence of ENSO on the IOD and vice versa—leads to the higher corr(N, IOD) in the REF case. The reason for the higher $\sigma(N)$ in REF compared with IODnoi is that in REF, the influence of ENSO on the IOD helps to let IOD events occur during a phase of the ENSO cycle where they in turn support ENSO development. These results confirm the hypothesis that a higher corr(N, IOD) leads to a stronger impact of the IOD on the spectral properties of ENSO but also suggest that the correlation between IOD and ENSO may partly be due to influence exerted by the Indian Ocean on the Pacific—not only vice versa. The high values of corr(N, IOB), however, must be dominated by the influence of N on the Indian Ocean because the influence of the IOB on the Pacific mainly counteracts ongoing ENSO events.

The relative independence of the IOD on the ENSO cycle makes it potentially a better ENSO predictor than the IOB, which is so closely linked to ENSO that it gives little additional information beyond what is already available from N (Izumo et al. 2014). To confirm this, we performed the "common cause test" of Wieners et al. (2016) on the data of the REF simulation. This test investigates whether the correlation between two time series z_2 and z_3 is significantly different from what one expects, given their correlations to a third time series z_1. In other words, it tests whether corr(z_2, z_3) can be explained by the fact that both z_2 and z_3 are also correlated to the common cause z_1. As argued in Wieners et al. (2016), the test is passed if both corr(Z_2, z_3) and corr(z_2, Z_3) are significant, where $Z_k = z_k - a_{k1}z_1 - b_{k1}$ and a_{k1}, b_{k1} are obtained from a linear fit of z_k onto z_1.

Here, we use IOD(t) or IOB(t) as z_2; $N(t + l_{23})$, where l_{23} is a positive lag, as z_3; and $N(t + l_{12})$, where $l_{12} \leq 0$, as z_1. That is, supposing that at time t we want to predict ENSO a time l_{23} in advance, we check if the IOD or IOB contains additional information compared to current or previous values of N, namely, at time $t + l_{12}$. As the value of l_{12} at which $N(t + l_{12})$ contains the most information about $N(t + l_{23})$ is not known a priori, we try every value in $l_{12} \in [-P, 0]$, where P is the ENSO period, and consider the test passed only if it is passed for each individual l_{12}.

The results for REF are given in Fig. 11. It can be seen that the IOB, despite reaching higher values of corr(z_2, z_3), never passes the test at 95% confidence (two tailed) except at two points, while the IOD reaches 99% significance for lags of about 4 months and

4 months $+ P/2$. At very small lags l_{23}, the test cannot be passed because then for $l_{12} = 0$, $N(t + l_{12})$ is automatically very similar to $N(t + l_{23})$, due to ENSO persistence. In the other simulations (not shown), the IOD always passes the common cause test for lags of about 4 months and 4 months $+ P/2$ at 99% significance (95% for IODnoi and IOB*2). For IOD*0, such a statement cannot be made. The IOB passes the common cause test at $l_{23} \approx 7$ months for the IOD*0.5 and IODnoi cases (95% confidence) and 99% for IOD*0 and the somewhat extreme case IOB*2—that is, mainly for those cases where corr(N, IOB) at small lags (see Table 5) are smaller than for REF, so that the IOB is less influenced by ENSO.

These results suggest that both the IOB and the IOD influence ENSO. The IOB has a stronger effect on the spectral properties of ENSO (damping and period shortening) because it is so strongly correlated to ENSO that its influence occurs at fixed phases of the ENSO cycle. The IOD enhances ENSO variability, hardly affects the period, and is—despite its much smaller wind response—a better ENSO predictor than the IOB because it is less strongly tied to the ENSO cycle. The IOB influence is dominated by the direct effect of the SST, but the strong IOD influence is made possible by the convergence-induced convection.

4. Summary, discussion, and conclusions

Based on a Gill-model response, one would expect that a cool western Indian Ocean is accompanied by westerly anomalies over the western Pacific. Our results suggest that a sufficiently strong convective feedback over the eastern Indian Ocean and Maritime Continent weakens, and may in principle even revert, this wind response into easterly anomalies, as illustrated in Fig. 1. This is because western Indian Ocean cooling leads to subsidence over the western Indian Ocean and (weak) upward motion above the Maritime Continent. The latter leads to condensation and convective heating, which in turn leads to stronger upward motion and horizontal mass convergence (i.e., easterlies over the western Pacific). This is in line with the proposed mechanism in Wieners et al. (2016). However, the reversal of the Gill response requires a very strong convection (i.e., a high value of γ_c), and it is not clear whether such values—or, in general, our simple representation of the convection—are realistic.

In observations, a cool western Indian Ocean in (boreal) autumn is often associated with a warm eastern Indian Ocean (Saji et al. 1999) and warm marginal seas in the Maritime Continent (Annamalai et al. 2010), thanks to the Indian Ocean dipole. As a warm eastern pole of the IOD can also lead to enhanced convection above the eastern Indian Ocean and Maritime Continent,
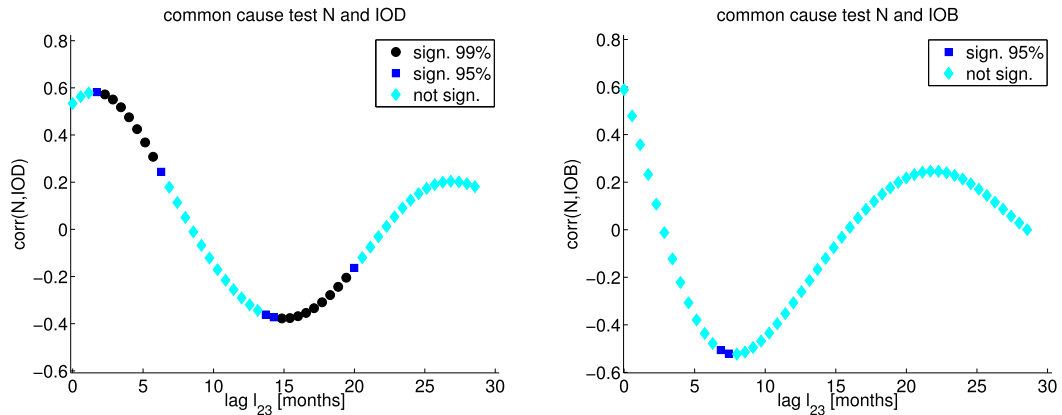
FIG. 11. Results of the common cause test for the REF simulation, using either the (left) IOD or (right) IOB as ENSO predictor. Black circles, dark blue squares, and light blue diamonds denote values that are significant at 99% confidence (two tailed), at 95% confidence, or not significant, respectively. The lag l_{23} is positive if the predictor (IOD or IOB) leads ENSO.

it is hard to disentangle the relative influence of both IOD poles. In fact, we find (Fig. 12, top row) that in our REF simulation the eastern IOD pole performs better than the western pole in the common cause test, although this is partially by design (i.e., choosing γ_c close to the value minimizing the wind impact of the western Indian Ocean). In observations, the western pole performs better (see Fig. 12, bottom). Whichever pole is dominant, we find that a negative IOD is associated with easterlies over the western Pacific, which can either support an ongoing La Niña (e.g., Annamalai et al. 2010) or enhance the western Pacific warm water volume to favor El Niño development after about 15 months (Izumo et al. 2010; Wieners et al. 2016). Our findings contradict studies suggesting that the IOD only has an indirect effect on ENSO, either by suppressing IOB variability, which has a damping effect on the ongoing ENSO (Annamalai et al. 2005; Santoso et al. 2012), or by strengthening (through removal of a delayed negative feedback) the effect of the spring IOB on next winter's ENSO (Izumo et al. 2015; note that our IOD corresponds to the "IOD+IOB" case in their Fig. 10e). These studies point out that as a result of their close proximity, the effects of the eastern and western pole of the IOD roughly cancel over the Pacific. Our results suggest that this is true for the direct SST heating effect but not for convergence-induced convection over the Maritime Continent.

The sensitivity studies in section 3c suggest that the net effect of Indian Ocean variability is to dampen ENSO and shorten its period, which is in line with many previous studies (Kug and Kang 2006; Kug et al. 2006; Santoso et al. 2012; Frauen and Dommenget 2012; Kajtar et al. 2017). The net effect of the Indian Ocean is dominated by the IOB, for which during El Niño we find that both the local heating and the convergence-induced

convection lead to easterlies opposing the westerlies associated with El Niño (Table 2). However, as the IOB is strongly correlated with ENSO (the correlation between Niño-3.4 in boreal winter and IOB in the following spring is about 0.85), the IOB does not offer ENSO-independent information and hence is not a useful precursor to ENSO (Izumo et al. 2014). On the other hand the IOD, which is less dependent on ENSO (the correlation between IOD in boreal autumn and Niño-3.4 in the following winter is about 0.6), may be a useful ENSO predictor, as suggested by Izumo et al. (2010). The correlation between IOD and N passes the common cause test, whereas the correlation between IOB and N hardly does (see Fig. 11).

Our results do not fully capture the mechanism of Indian Ocean–ENSO interaction suggested by Izumo et al. (2010) and Wieners et al. (2016), wherein a cool western Indian Ocean or negative IOD favors El Niño after 15 months. Rather, a negative IOD is followed by La Niña after just a few months. In observations, IOD variability is typically highest in boreal autumn, which is too late in the year to induce a major La Niña [although Luo et al. (2010) suggest that a cool IODe early in the season may support El Niño growth]; instead, the IOD-induced easterlies lead to an increased western Pacific warm water volume, which favors El Niño in the following year. Our model lacks a seasonal cycle and its ENSO period is too short; therefore, it does not capture this delay between IOD forcing and ENSO variability. However, a vital process—the easterly wind response to negative IOD forcing due to convection over the Maritime Continent—is represented.

As mentioned, a source of uncertainty in our model is the value of the convection parameter γ_c. For values around $\gamma_c = 1.02c_a^2$ (where the wind response to the western Indian Ocean heating switches sign) the results become rather
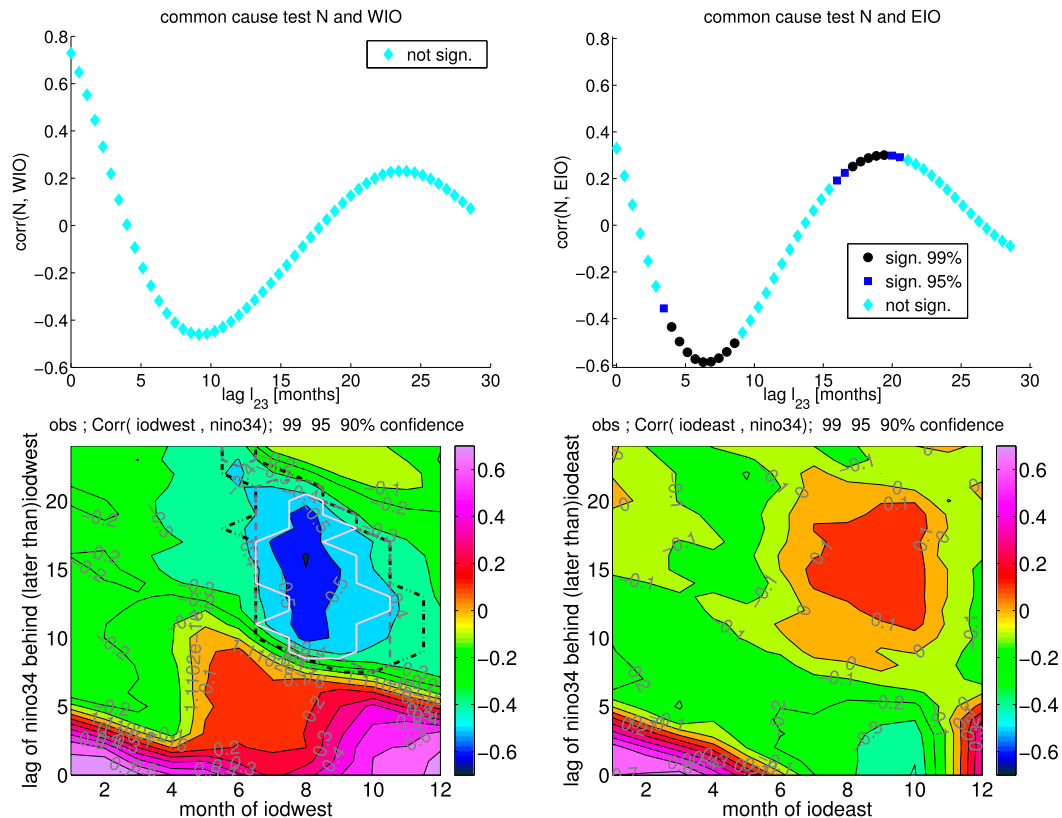
FIG. 12. (top) Model results of the common cause test for the REF simulation, using either the (left) WIO or (right) EIO as ENSO predictor. Black circles, dark blue squares, and light blue diamonds denote values that are significant at 99% confidence (two tailed), at 95% confidence, or not significant, respectively. The lag l_{23} is positive if the predictor (IOD or IOB) leads ENSO. (bottom) As in (top), but for observations. Since observations have a seasonal cycle, each month is treated separately: the x axis represents the month where the IODw or IODe is taken (1 being January, etc.), the y axis shows the lag l_{23}, which is positive if the Indian Ocean leads. Black dotted–dashed, gray dashed, and white solid lines encircle areas where the common cause test is passed with 90%, 95%, and 99% confidence, respectively.

sensitive to γ_c; hence, it is hard to assess whether our value is "correct." If the high sensitivity to γ_c is not solely due to our very simple convection scheme, our results strengthen the notion that a good representation of convection is important for correct modeling of ENSO and its interaction with the Indian Ocean. With our model we can only show that convection over the Maritime Continent *might* have an important effect. Note that even if in reality the convection effect were too weak to turn the wind response over the Pacific to a pure cool western Indian Ocean into easterlies, it might still lead to a easterly response to a negative IOD, for which the pure Gill response is nearly zero.

It is maybe impossible to judge from observations whether the convection feedback can turn the Pacific wind response to a cool western Indian Ocean into easterlies because of the powerful ENSO cycle obscuring the Indian Ocean–induced signals. Therefore, experiments with more sophisticated models are needed to check our findings. Kajtar et al. (2017) performed partial

decoupling experiments with a relatively low-resolution AOGCM. In their Figs. 8a,e, they show that for their fully coupled simulation a composite of positive (negative) IOD years is accompanied by strong westerlies (easterlies) over the Pacific for more than half a year. When suppressing interannual Pacific variability, most of this signal vanishes, but there remains a spatially confined but statistically significant westerly (easterly) signal in late boreal autumn (see their Figs. 8b,f; although the latter signal is only very weak). These signals might be a result of Indian Ocean–induced nonlinear convection over the Maritime Continent. Note, many GCMs still have biases in modeling the IOD (Cai and Cowan 2013), which may affect the simulation of such subtle effects as IOD–ENSO interaction.

Our results suggest that convection above the Maritime Continent may play an important role in interactions between the Indian Ocean and ENSO; nonlocally induced convection might even reverse the wind direction
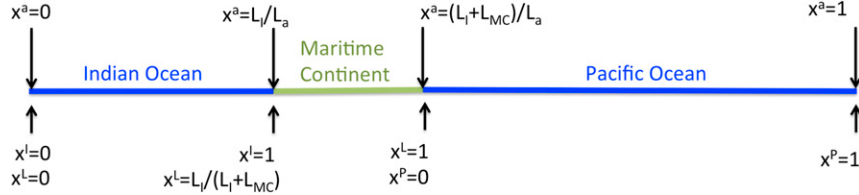
FIG. A1. Illustration of the nondimensional zonal coordinates. The lengths L_I, L_{MC}, L_P are as defined in Fig. 2.

on the atmospheric bridge. It might hence be worthwhile to study these processes with more sophisticated models. This may also be of value for understanding future changes in the Indian Ocean–ENSO interaction, since convection anomalies might be rather sensitive to changes in the warm pool background state.

APPENDIX

Implementation of the Convective Heating

A detailed description of the convection-free model and its implicit, pseudospectral implementation is given in Wieners et al. (2017); therefore, here we will focus on the implementation of the convection feedback.

In this appendix all quantities are nondimensional, using the same scales as in Wieners et al. (2017). The nondimensional zonal coordinates are illustrated in Fig. A1. Atmospheric divergence is scaled with c_a/L_a. The convection-free model is discretized using a pseudospectral method. The Pacific component of the model has two sets of independent variables; namely, $Q^T = (\alpha_T L_a \Delta T/c_a^3)(T - T_0) \equiv \tilde{\alpha}_T(T - T_0)$, the nondimensional SST-induced heating, and $r = (u^r + h)/2$, where u^r and h are the zonal reduced gravity velocity and thermocline depth deviation, respectively. These quantities are decomposed as

$$Q^T(x^P, y^P) = \sum_{ij} f_{ij}(x^P, y^P)q_{ij}^T, \, r(x^P, y^P) = \sum_{ij} f_{ij}(x^P, y^P)r_{ij},$$

(A1)

with the shorthand $\sum_{ij} \equiv \sum_{i=0}^{n_x}\sum_{j=0}^{n_y}$. The functions f_{ij} are given by

$$f_{ij} = \tilde{C}_i(x^P)\psi_j(y^P),$$

where $\tilde{C}_i(x) = C_i(2x - 1)$ with C_i being the ith Chebyshev polynomial and ψ_j the jth Hermitian function. The f_{ij} form an orthogonal basis. Together with the n_I Indian Ocean (IO) SST amplitudes A_m, the q_{ij}^T and r_{ij} form the $2(n_x + 1)(n_y + 1) + n_I$-dimensional space vector $\mathbf{z} = (r_{ij}, q_{ij}^T, A_m)$.

The variables are evaluated at the collocation points (x_k^P, y_l^P) with k and l ranging from 0 to n_x and n_y, respectively, and $x_k^P = 2[1 - \cos(\pi k/n_x)]$ and y_l^P is the lth root of the $(n_y + 1)$th Hermitian function. We introduce a shorthand, $Q_{kl}^T = Q^T(x_k^P, y_l^P)$. Now with a finite number of base functions and collocation points, (A1) actually amounts to a matrix multiplication:

$$Q_{kl}^T = \sum_{ij} F_{kl,ij}q_{ij}^T$$

with $F_{kl,ij} = f_{ij}(x_k^P, y_l^P)$. The decomposition is a bijection; hence one can also write

$$q_{ij}^T = \sum_{kl} P_{ij,kl}Q_{kl}^T,$$

where P is the inverse of F.

Winds at the (k, l)th Pacific collocation point are very efficiently computed from the heating coefficients q_{ij}^T and the amplitudes A_m of the mth IO SST pattern:

$$(u_{kl}^a, v_{kl}^a) = \sum_{ij}(\mathcal{A}_{kl,ij}, \mathcal{B}_{kl,ij})q_{ij}^T + \sum_{m=1}^{n_I}(\mathcal{A}_{kl,m}^I, \mathcal{B}_{kl,m}^I)A_m,$$

(A2)

where $\mathcal{A}_{kl,ij}$ and $\mathcal{B}_{kl,ij}$ are the zonal and meridional wind at the (k, l)th Pacific collocation point in case only the SST mode ij is excited ($q_{ij}^T = 1$), and $(\mathcal{A}_{kl,m}^I, \mathcal{B}_{kl,m}^I)$ are the contributions of the mth IO SST pattern. Winds over the IO or Maritime Continent (MC) need not be computed, as they have no effect (no ocean dynamics can be forced by wind here).

In Zebiak and Cane (1987), the convection feedback is computed iteratively. In our implicit implementation of the model, this would require numerical approximations of the Jacobian. Instead, we add the divergence

$c = \partial_{x^a} u^a + \partial_{y^a} v^a$ to the state vector, which takes the form $\mathbf{z} = (r_{ij}, q_{ij}^T, c_{ij}, A_k)$. This requires additional, implicit diagnostic equations for c.

The divergence needs to be defined both on Pacific collocation points and over the IO and MC because convective heating over the IO or MC can lead to wind anomalies over the Pacific. The IO and MC can be mathematically treated as one entity because their surface temperature is not determined by ocean dynamics but parameterized. Hence, they will collectively be referred to as "land." A superscript L is used to indicate that a quantity is defined over land.

Grid points over land have the same y coordinates as over sea (i.e., the Pacific), whereas in the x direction, $n_x^L + 1 = 18$ equidistant points are used. Their nondimensional atmospheric coordinates are $x_k^a = [k(L_I + L_{MC})/n_x^L L_a]$; $k \in \{0, 1, \ldots, n_x^L\}$. The base functions over land are of the form

$$f_{ij}^L(x^L, y^L) = \psi_j(y^L) \times \begin{cases} 1 & \text{if} \quad i = 0 \\ \cos(2\pi m x^L) & \text{if} \quad i = 2m - 1; m \in \{1, \ldots, N_c\}, \\ \sin(2\pi m x^L) & \text{if} \quad i = 2m; m \in \{1, \ldots, N_s\} \end{cases}$$

where $(N_c, N_s) = [(n_x^L + 1)/2, (n_x^L - 1)/2]$ for odd n_x^L and $(N_c, N_s) = [(n_x^L)/2, (n_x^L)/2]$ for even n_x^L. With these base functions, SST- or convection-induced heating over land can be decomposed in the same way as over the Pacific:

$$Q_{kl}^{LT} = \sum_{ij} F_{kl,ij}^L q_{ij}^{LT}, q_{ij}^{LT} = \sum_{kl} P_{ij,kl}^L Q_{kl}^{LT} \quad \text{and}$$

$$Q_{kl}^{Lc} = \sum_{ij} F_{kl,ij}^L q_{ij}^{Lc}, q_{ij}^{Lc} = \sum_{kl} P_{ij,kl}^L Q_{kl}^{Lc},$$

where $F_{kl,ij}^L = f_{ij}^L(x_k^L, y_l^L)$, P^L is the inverse of F^L, and Q^{LT} is determined by the prescribed IO SST patterns: $Q_{kl}^{LT} = \tilde{\alpha}_T \sum_{m=1}^{n_I} T_m^{0I}(x_k^L y_l^L) A_m$. These projections of surface temperature and convection induced heating make it possible to keep using the efficient computation of winds and divergence in terms of the q_{ij}, similar to (A2).

Now it is possible to write the wind divergence in a similar fashion as (A2), only that the divergence is needed both above land and above sea. As for the wind, the divergence is influenced by heating both over land and over sea.

The divergence over sea becomes

$$c_{kl} = \sum_{ij} \mathcal{C}_{kl,ij}^{PP}(q_{ij}^T + q_{ij}^c) + \sum_{ij} \mathcal{C}_{kl,ij}^{PL}(q_{ij}^{LT} + q_{ij}^{Lc}), \quad \text{(A3)}$$

where $\mathcal{C}_{kl,ij}^{PP}$ and $\mathcal{C}_{kl,ij}^{PL}$ are the wind divergence in the Pacific location (x_k^P, y_l^P) caused by heating associated with the ijth base function in the Pacific and over land, respectively. Analogously the divergence over land becomes

$$c_{kl}^L = \sum_{ij} \mathcal{C}_{kl,ij}^{LP}(q_{ij}^T + q_{ij}^c) + \sum_{ij} \mathcal{C}_{kl,ij}^{LL}(q_{ij}^{LT} + q_{ij}^{Lc}). \quad \text{(A4)}$$

As the convection feedback has a tendency to amplify short-scale features, a slight spatial smoothing has been applied to the $\mathcal{C}$ (e.g., over sea, $\mathcal{C}$ would be a smoothed version of $\partial_{x^a}\mathcal{A} + \partial_{y^a}\mathcal{B}$).

Now we use $Q_{kl}^c = \hat{a}_\kappa \tilde{\gamma}_c m_{kl}[\mathcal{M}(-c_{kl} - c_{kl}^b)]^{\hat{\kappa}} - \hat{b}_\kappa$ over sea and $Q_{kl}^{Lc} = \hat{a}_\kappa \tilde{\gamma}_c m_{kl}^L[\mathcal{M}(-c_{kl}^L - c_{kl}^{Lb})]^{\hat{\kappa}} - \hat{b}_\kappa$ over land (see section 2b), where $\tilde{\gamma}_c = \gamma_c/c_a^2$ is the nondimensional equivalent of γ_c and $(\hat{a}_\kappa, \hat{b}_\kappa, \tilde{a}_\kappa)$ takes the values $(1, 0, \kappa)$ if $-c_{kl} - c_{kl}^b < C_0$ and $(a_\kappa, b_\kappa, \tilde{\kappa})$ else [see (4)]. This yields implicit, diagnostic equations for the state variables c_{kl} and c_{kl}^L:

$$c_{kl} = \sum_{ij} \mathcal{C}_{kl,ij}^{PP}\left(q_{ij}^T + \sum_{k'l'} P_{ij,k'l'}\{\hat{a}_\kappa \tilde{\gamma}_c m_{k'l'}[\mathcal{M}(-c_{k'l'} - c_{k'l'}^b)]^{\hat{\kappa}} - \hat{b}_\kappa\}\right)$$

$$+ \sum_{ij} \mathcal{C}_{kl,ij}^{PL}\left(q_{ij}^{LT} + \sum_{k'l'} P_{ij,k'l'}^L\{\hat{a}_\kappa \tilde{\gamma}_c m_{k'l'}^L[\mathcal{M}(-c_{k'l'}^L - c_{k'l'}^{Lb})]^{\hat{\kappa}} - \hat{b}_\kappa\}\right) \quad \text{and}$$

$$c_{kl}^L = \sum_{ij} \mathcal{C}_{kl,ij}^{LP}\left(q_{ij}^T + \sum_{k'l'} P_{ij,k'l'}\{\hat{a}_\kappa \tilde{\gamma}_c m_{k'l'}[\mathcal{M}(-c_{k'l'} - c_{k'l'}^b)]^{\hat{\kappa}} - \hat{b}_\kappa\}\right)$$

$$+ \sum_{ij} \mathcal{C}_{kl,ij}^{LL}\left(q_{ij}^{LT} + \sum_{k'l'} P_{ij,k'l'}^L\{\hat{a}_\kappa \tilde{\gamma}_c m_{k'l'}^L[\mathcal{M}(-c_{k'l'}^L - c_{k'l'}^{Lb})]^{\hat{\kappa}} - \hat{b}_\kappa\}\right). \quad \text{(A5)}$$

The equations for the total wind over the Pacific have to be extended with the convective heating contribution:

$$(u_{kl}^a, v_{kl}^a) = \sum_{ij} (\mathcal{A}_{kl,ij}^{PP}, \mathcal{B}_{kl,ij}^{PP})(q_{ij}^T + q_{ij}^c)$$
$$+ \sum_{ij} (\mathcal{A}_{kl,ij}^{PL}, \mathcal{B}_{kl,ij}^{PL})(q_{ij}^{LT} + q_{ij}^{Lc}).$$

The winds over land have no influence on any dynamics and are not explicitly computed.

REFERENCES

Anderson, D. L. T., and J. P. J. McCreary, 1985: On the role of the Indian Ocean in a coupled ocean–atmosphere model of El Niño and the Southern Oscillation. *J. Atmos. Sci.*, **42**, 2439–2442, doi:10.1175/1520-0469(1985)042<2439:OTROTI>2.0.CO;2.

Annamalai, H., S.-P. Xie, and J. P. J. McCreary, 2005: Impact of Indian Ocean sea surface temperature on developing El Niño. *J. Climate*, **18**, 302–319, doi:10.1175/JCLI-3268.1.

——, S. Kida, and J. Hafner, 2010: Potential impact of the Indian Ocean–Indonesian Seas on El Niño. *Geophys. Res. Lett.*, **40**, 1200–1205, doi:10.1175/2010JCLI3396.1.

Cai, W., and T. Cowan, 2013: Why is the amplitude of the Indian Ocean dipole overly large in CMIP3 and CMIP5 climate models? *Nature*, **443**, 324–328, doi:10.1002/grl.50208.

Frauen, C., and D. Dommenget, 2012: Influences of the tropical Indian and Atlantic Oceans on the predictability of ENSO. *Geophys. Res. Lett.*, **39**, L02706, doi:10.1029/2011GL050520.

Gadgil, S., P. V. Joseph, and N. V. Joshi, 1984: Ocean–atmosphere coupling over monsoon regions. *Nature*, **312**, 141–143, doi:10.1038/312141a0.

Gill, A. E., 1980: Some simple solutions for heat-induced tropical circulation. *Quart. J. Roy. Meteor. Soc.*, **106**, 447–462, doi:10.1002/qj.49710644905.

Izumo, T., J. Vialard, M. Lengaigne, C. de Boyer Montégut, S. K. Behera, J.-J. Luo, and Coauthors, 2010: Influence of the state of the Indian Ocean dipole on the following year's El Niño. *Nat. Geosci.*, **3**, 168–172, doi:10.1038/ngeo760.

——, M. Lengaigne, J. Vialard, J.-J. Luo, T. Yamagata, and G. Madec, 2014: Influence of Indian Ocean dipole and Pacific recharge on following year's El Niño: Interdecadal robustness. *Climate Dyn.*, **42**, 291–310, doi:10.1007/s00382-012-1628-1.

——, J. Vialard, H. Dayan, M. Lengaigne, and I. Suresh, 2015: A simple estimation of equatorial Pacific response from wind-stress to untangle Indian Ocean dipole and basin influences on El Niño. *Climate Dyn.*, **46**, 2247–2268, doi:10.1007/s00382-015-2700-4.

Jin, F.-F., 1997: An equatorial ocean recharge paradigm for ENSO. Part II: A stripped-down coupled model. *J. Atmos. Sci.*, **54**, 830–847, doi:10.1175/1520-0469(1997)054<0830:AEORPF>2.0.CO;2.

Kajtar, J. B., A. Santoso, M. H. England, and W. Cai, 2017: Tropical climate variability: Interactions across the Pacific, Indian, and Atlantic Oceans. *Climate Dyn.*, **48**, 2173–2190, doi:10.1007/s00382-016-3199-z.

Keller, H. B., 1977: Numerical solution of bifurcation and non-linear eigenvalue problems. *Applications of Bifurcation Theory*, P. Rabinowitz, Ed., Academic Press, 359–384.

Klein, S. A., B. J. Soden, and N. C. Lau, 1999: Remote sea surface temperature variations during ENSO: Evidence for a tropical atmospheric bridge. *J. Climate*, **12**, 917–932, https://doi.org/10.1175/1520-0442(1999)012<0917:RSSTVD>2.0.CO;2.

Kug, J. S., and I.-S. Kang, 2006: Interactive feedback between ENSO and the Indian Ocean. *J. Climate*, **19**, 1784–1801, doi:10.1175/JCLI3660.1.

——, T. Li, S.-I. An, I.-S. Kang, J.-J. Luo, S. Masson, and T. Yamagata, 2006: Role of the ENSO–Indian Ocean coupling on ENSO variability in a coupled GCM. *Geophys. Res. Lett.*, **33**, L09710, doi:10.1029/2005GL024916.

Luo, J.-J., R. Zhang, S. K. Behera, Y. Masumoto, F.-F. Jin, R. Lukas, and T. Yamagata, 2010: Interaction between El Niño and extreme Indian Ocean dipole. *J. Climate*, **23**, 726–742, doi:10.1175/2009JCLI3104.1.

Meinen, C. S., and M. J. McPhaden, 2000: Observations of warm water volume changes in the equatorial Pacific and their relationship to El Niño and La Niña. *J. Climate*, **13**, 3551–3559, doi:10.1175/1520-0442(2000)013<3551:OOWWVC>2.0.CO;2.

Met Office, 2017: Hadley Centre Sea Ice and Sea Surface Temperature data set (HadISST). Met Office Hadley Centre, accessed 14 February 2017, http://www.metoffice.gov.uk/hadobs/hadisst/.

Neelin, J. D., D. S. Battisti, A. C. Hirst, F.-F. Jin, Y. Wakata, T. Yamagata, and S. E. Zebiak, 1998: ENSO theory. *J. Geophys. Res.*, **103**, 14 261–14 290, doi:10.1029/97JC03424.

Philander, S. G., 1990: *El Niño, La Niña, and the Southern Oscillation*. Academic Press, 289 pp.

Rayner, N. A., and Coauthors, 2003: Global analyses of sea surface temperature, sea ice, and night marine air temperature since the late nineteenth century. *J. Geophys. Res.*, **108**, 4407, doi:10.1029/2002JD002670.

Roxy, M., 2013: Sensitivity of precipitation to sea surface temperature over the tropical summer monsoon region—and its quantification. *Climate Dyn.*, **4**, 1159–1169, doi:10.1007/s00382-013-1881-y.

Saji, H. N., B. N. Goswami, P. N. Vinayachandran, and T. Yamagata, 1999: A dipole mode in the tropical Indian Ocean. *Nature*, **401**, 360–363.

——, S.-P. Xie, and T. Yamagata, 2006: Tropical Indian Ocean variability in the IPCC twentieth-century climate. *J. Climate*, **19**, 4397–4317, doi:10.1175/JCLI3847.1.

Santoso, A., M. H. England, and W. Cai, 2012: Impact of Indo-Pacific feedback interactions on ENSO dynamics diagnosed using ensemble climate simulations. *J. Climate*, **25**, 7743–7763, doi:10.1175/JCLI-D-11-00287.1.

Schott, F. A., S.-P. Xie, and J. P. J. McCreary, 2009: Indian Ocean circulation and climate variability. *Rev. Geophys.*, **47**, RG1002, doi:10.1029/2007RG000245.

Shinoda, T., H. H. Hendon, and M. A. Alexander, 2004: Surface and subsurface dipole variability in the Indian Ocean and its relation with ENSO. *Deep-Sea Res. I*, **51**, 619–635, doi:10.1016/j.dsr.2004.01.005.

van der Vaart, P. C. F., H. A. Dijkstra, and F.-F. Jin, 2000: The Pacific cold tongue and the ENSO Mode: A unified theory within the Zebiak–Cane model. *J. Atmos. Sci.*, **57**, 967–988, doi:10.1175/1520-0469(2000)057<0967:TPCTAT>2.0.CO;2.

Watanabe, M., 2008: Two regimes of the equatorial warm pool. Part I: A simple tropical climate model. *J. Climate*, **21**, 3533–3544, doi:10.1175/2007JCLI2151.1.

——, and F.-F. Jin, 2002: Role of Indian Ocean warming in the development of Philippine Sea anticyclone during ENSO. *Geophys. Res. Lett.*, **29**, 1121–1139, doi:10.1029/2001GL014318.

——, and ——, 2003: A moist linear baroclinic model: Coupled dynamical–convective response to El Niño. *J. Climate*, **16**, 1121–1139, https://doi.org/10.1175/1520-0442(2003)16<1121:AMLBMC>2.0.CO;2.

Webster, P. J., A. M. Moore, J. P. Loschnigg, and R. R. Leben, 1999: Coupled ocean–atmosphere dynamics in the Indian Ocean during 1997–98. *Nature*, **401**, 356–360, doi:10.1038/43848.

Wieners, C. E., W. P. M. de Ruijter, W. Ridderinkhof, A. von der Heydt, and H. Dijkstra, 2016: Coherent tropical Indo-Pacific interannual climate variability. *J. Climate*, **29**, 4269–4291, doi:10.1175/JCLI-D-15-0262.1.

——, ——, and H. A. Dijkstra, 2017: The influence of the Indian Ocean on ENSO stability and flavour. *J. Climate*, **30**, 2601–2620, doi:10.1175/JCLI-D-16-0516.1.

Wyrtki, K., 1975: El Niño—The dynamic response of the equatorial Pacific Ocean to atmospheric forcing. *J. Phys. Oceanogr.*, **5**, 572–584, doi:10.1175/1520-0485(1975)005<0572:ENTDRO>2.0.CO;2.

Xie, S.-P., K. Hu, J. Hafner, H. Tokinaga, Y. Du, G. Huang, and T. Sampe, 2009: Indian Ocean capacitor effect on Indo–western Pacific climate during the summer following El Niño. *J. Climate*, **22**, 730–747, doi:10.1175/2008JCLI2544.1.

Zebiak, S. E., 1986: Atmospheric convergence feedback in a simple model for El Niño. *Mon. Wea. Rev.*, **114**, 1263–1271, doi:10.1175/1520-0493(1986)114<1263:ACFIAS>2.0.CO;2.

——, and M. A. Cane, 1987: A model El Niño–Southern Oscillation. *Mon. Wea. Rev.*, **115**, 2262–2278, doi:10.1175/1520-0493(1987)115<2262:AMENO>2.0.CO;2.